Full Waveform Inversion Guided Wave Tomography Based on Recurrent Neural Network

Master's thesis (Tech.)
University of Turku
Department of Future Technologies
2022
Zijian Wang

Supervisors:
MSc. Sahar Salimpour Kasebi
Assoc. Prof. Dan Li

UNIVERSITY OF TURKU
Department of Future Technologies

WANG ZIJIAN: Full Waveform Inversion Guided Wave Tomography Based on Recurrent Neural Network, 68 p.
Computer Systems
August 2022

Corrosion quantitative detection of plate or plate-like structures is a critical and challenging topic in industrial Non-Destructive Testing (NDT) research which determines the remaining life of material. Compared with other methods (X-ray, magnetic powder, eddy current), ultrasonic guided wave tomography has the advantages of non-invasiveness, high efficiency, high precision and low cost. Among various ultrasonic guided wave tomography algorithms, travel time or diffraction algorithms can be used to reconstruct defect or corrosion model, but the accuracy is low and heavily influenced by the noise. Full Waveform Inversion (FWI) can build accurate reconstructions of physical properties in plate structures, however, it requires a relatively accurate initial model, and there is still room for improvement in the convergence speed, imaging resolution and robustness.

This thesis starting with the physical principle of ultrasonic guided waves, the dispersion characteristic curve of the guided wave propagating in the plate structure converts the change of the remaining thickness of the plate structure material into the wave velocity variation when the ultrasonic guided wave propagates in it, and provides a physical principle for obtaining the thickness distribution map from the velocity reconstruction. Secondly, a guided wave tomography method based on Recurrent Neural Network Full Waveform Inversion (RNN-FWI) is proposed. Finally, the efficiency of the above method is verified through practical experiments. The main work of the thesis includes:

- The feasibility of conventional full waveform inversion for guided wave tomography is introduced and verified.
- An FWI algorithm based on RNN is proposed. In the framework of RNN-FWI, the effects of different optimization algorithms on imaging performance and the effects of different sensor numbers and positions on imaging performance are analyzed.
- The quadratic Wasserstein distance is used as the objective equation to further reduce the dependence on the initial model. The depth image prior (DIP) based on convolutional neural network (CNN) is used as the regularization method to further improve the conventional FWI algorithm, and the effectiveness of the improved algorithm is verified by simulation and actual experiments.

Keywords: Full waveform inversion (FWI); guided wave tomography; Recurrent Neural Network

Content

Chapter 1 Introduction

1.1 Research background and significance

Plates or plate-like components are widely utilized in the aircraft, car, shipbuilding, and petroleum industries, as well as pressure and chemical containers. However, defects like corrosion, cavitation, and wear introduced during manufacturing and operation would jeopardize the system's overall safety [1]. Simultaneously, due to the effect of mechanic and chemistry on the plates, an expansion of small defect inside the plate may trigger the fatigue failure, resulting in production safety accident. Two examples of corrosion on storage tanks are presented in Figure 1.1 [2]. In 2006, a leak incident from corroded pipe spilled more than 200,000 gallons of oil in Alaska [3], causing serious contamination to the environment and leading to a $20 million fine to the company involved. Therefore, the damage detection of the plate and the quantitation of the remaining life of materials are very critical. In reality, most of the thin plates work in environments that are difficult to access by ordinary detection instruments, and some conventional detection methods have low detection efficiency, intrusive transducers, and poor precision. These shortcomings are not tolerated by the modern industry; therefore, non-destructive testing of such plate-shaped components is highly required. As one of the five conventional non-destructive testing technologies, ultrasonic non-destructive testing technology is often used to detect defects inside of material. Due to its strong detection ability, it can even penetrate deep into the metal several meters depth. Moreover, the ultrasonic intensity acting on the material is sufficiently low, and the maximum excitation stress is far lower than the elastic limit of the material. In addition, the equipment requirement is simple, and do no harm or pollution to the workpiece and the surrounding environment [4].

(a) (b)

Figure 1.1 (a) Corrosion on the bottom of a crude oil storage tank, (b) corrosion on the gas oil aboveground storage tank.

Ultrasonic testing is to make ultrasonic waves enter the test piece, and study the reflected, transmitted and scattered waves through the interaction between the ultrasonic wave and the test piece, so as to carry out macroscopic defect detection on the test piece. Ultrasonic nondestructive testing is commonly used for longitudinal wave (compression wave) and transverse wave (shear wave) detection, but for thin plates, it is difficult to detect transverse waves or longitudinal waves. In fact, whether the transverse wave is obliquely incident or the longitudinal wave is vertically incident into the thin plate, when the ultrasonic wave propagates for a certain distance, the ultrasonic wave at this time is no longer an ordinary transverse wave or longitudinal wave due to the continuous reflection of the upper and lower surfaces of the thin plate, but a new type of ultrasonic wave, that is, a lamb wave [5]. This new non-destructive method analyzes lamb waveform signals variations when passing through defects in the test piece, such as reflection, transmission, and scattering, and utilizes lamb wave dispersion characteristics to translate the speed map into the remaining thickness for the corrosion quantitatively. Lamb wave is the most common form of guided wave in ultrasonic nondestructive testing. Unlike conventional ultrasonic point-by-point scanning, Lamb wave testing scans one line at a time, and the transceiver probe can be placed on the same side of the specimen. It is convenient in different situations, so Lamb wave detection has the characteristics of fast and efficient incomparable with longitudinal wave and transverse wave for non-destructive testing of thin plates, and it is very suitable for large-area non-destructive testing of plate-shaped structures [6].

Although the non-destructive testing of metal sheets is the earliest application area of Lamb wave technology. However, due to the complexity of the Lamb wave theory and detection mechanism, this technology has not yet achieved a major breakthrough, and there are still many inconsistent views and unsolved problems, such as the scattering mechanism of Lamb waves by delamination, and how to choose the best detection parameters, how to overcome the sometimes-possible layered missed inspection, how to perform qualitative and quantitative analysis of defects and selection of artificial defects [7], all of which greatly limit its application in industrial production. The American Society for Testing and Materials (ASTM) and the Aerospace Materials Specification (AMS) both propose that Lamb waves can be used for flaw detection of metal sheets, but the specific implementation methods are not involved [8]. Due to the complexity of the Lamb wave propagation and reflection mechanism, foreign countries have not yet formulated relevant standards for Lamb wave nondestructive testing. Although two national standards and one professional standard have been formulated in China [9-11], but this does not mean that these issues have been properly resolved, there are still many controversial and even wrong places in these standards. The research on Lamb wave non-destructive testing technology in sheet metal is the foundation, which is of great significance for the further application of Lamb wave.

1.2 Progress in research at home and abroad

1.2.1 Lamb wave non-destructive testing technology for plate metal

Lamb waves were discovered in 1917. At that time, the British mechanician H. Lamb solved the wave formula according to the free boundary conditions of the plate, and obtained a special wave solution [12]. Later researchers named this wave lamb wave in honor of its discoverer. Ultrasonic lamb wave is a special form of stress wave synthesized by longitudinal and transverse waves in an acoustic waveguide whose thickness is the same order of magnitude as the excitation acoustic wave wavelength (such as a metal sheet) [13]. It produces different propagation modes under different thicknesses and different excitation frequencies. There are two types of lamb waves:

symmetric lamb and anti-symmetric lamb, and there are many modes corresponding to each type. It is a guided wave in a plate, also commonly referred to as a "plate wave". Plate wave is a general term. When the upper and lower interfaces of the plate are mechanically free, this special wave is called lamb wave [14]. Early researches on non-destructive testing and non-destructive evaluation of lamb waves mainly focused on homogeneous and isotropic media [15].

In the late 1940s, American F. Firestone (who is also the inventor of ultrasonic flaw detection) first applied lamb waves to thin plate flaw detection. Later, D.C. Worlton [16], an engineer from the General Electric Company of the United States, first pointed out that the mode characteristics of the dispersion curves of aluminum and zirconium can be applied to non-destructive testing of materials. However, the imperfection of lamb wave propagation theory greatly limits its application. Many researchers have done a lot of work on this. H. Lamb and J. Rayleigh[17] derived the Rayleigh-Lamb transcendental formula in the isotropic plate in free state, and theoretically analyzed the propagation characteristics of Lamb waves. A. Love[18] and J. Rayleigh studied the propagation mode and characteristics of Lamb waves based on the classical plate and shell theory. R. Cooper and L. Mirsky et al. [19] focused on the propagation theory of Lamb waves, and further revised and improved the frequency characteristic formula of Lamb waves. In the 1970s, Sachse et al. applied the Fourier transform method to study the dispersion characteristics of Lamb waves, and used the time-frequency analysis method to measure the wave numbers and phase velocities of Lamb waves at different frequencies [20]. The group velocity dispersion curve of the Lamb wave low-frequency mode (A0, S0) is calculated by PS/PR technology [21]. P. Cawly et al. [22] used finite element analysis to analyze the dispersion curve of the Lamb wave in low-order mode, and applied the two-dimensional Fourier transform method to experimentally measure the phase velocity dispersion curve of the Lamb wave with different frequencies and thicknesses of the steel plate, and then the time-frequency analysis method is also used, focusing on the analysis of the low-order modes A0, S0 [23].

In recent years, Lamb waves have been widely used in the mechanical safety

testing of isotropic and anisotropic materials [24]. In 2008, A. Rohde et al. obtained information such as thickness, density and Young's modulus of the plate by performing diffraction tomography on the plate under the Born hypothesis [25]. From 2008 to 2010, P. Belanger and P. Cawley et al. studied the thickness measurement of the corrosion region based on Lamb wave tomography [26].

In China, domestic research on Lamb wave tomography is gradually increasing. Lan et al of the Wuhan Institute of Physics, Chinese Academy of Sciences studied the principle of ultrasonic tomography, developed a set of ultrasonic reflection tomography experimental equipment [27]. C. F. Ying et al of the Institute of Acoustics of the Chinese Academy of Sciences used the photo-elastic method to directly observe the stress distribution of Lamb waves, which is the first time in the world to directly observe the stress distribution of Lamb waves [14]. Z. Q. Liu et al from the Institute of Acoustics of Tongji University used two-dimensional Fourier transform to study the Lamb wave mode identification and phase velocity detection, and identified the propagating Lamb wave mode to a certain extent [28]. Z. Q. Huang et al from Tsinghua University used electromagnetic ultrasound to excite A0 mode Lamb waves, and used cross-hole scanning to image defects with a diameter of 30mm and a depth of 2mm on a 3mm aluminum plate. However, the final imaging effect has obvious artifacts and needs to be further improved [29].

At the moment, guided wave tomography approaches include travel-time tomography, which is based on the straight or bent ray, diffraction tomography, and hybrid algorithms combining the first two, such as Mindlin plate theory, HARBUT and full waveform inversion.

Travel time tomography estimates the velocity map of a straight ray model-based structure by inverting the travel time of an ultrasonic guided wave [30]. However, straight ray propagation-based algorithms neglect bent ray and diffraction, only low-contrast and large defects can be detected [31], which limited by the first Fresnel zone width $\sqrt{L\lambda}$, where L is the ray path length from source to receiver and λ is the lamb center frequency wavelength. Bent rays and diffraction must be considered to increase

the resolution [32]. Although diffraction tomography reaches the resolution of half wavelength, it is still constrained by the born approximation's weakness, which only low contrast defects and high SNR signals are suitable for the case.

However, algorithms solely based on straight, bent ray or diffraction has certain limits, thus the research community has proposed numerous hybrid techniques to improve resolution. For example, P. Huthwaite et al. [33-35] introduced the HARBUT algorithm, which considered straight, bent ray, and diffraction, and used corrected born approximation, to ensure diffraction tomography accuracy and to no longer be limited by defect contrast. However, HARBUT, on the other hand, did not take higher-order scatterings into account.

The Mindlin plate theory [51] can capture the scattering of guided waves, which provided an approximation model of A0 mode guided wave with dispersive properties by neglecting thickness of plate-like materials and transformed the three-dimensional (3-D) problem in a simplified two dimensional (2-D) equivalent model. But in this way, only small thickness loss could be detected because it also based on Born approximation.

1.2.2 Research status of full waveform inversion method

The Full Waveform Inversion (FWI), which is based on solving the acoustic or elastic wave formula, is a feasible high-resolution algorithm. The FWI method is a geophysical technique that is commonly utilized in geological exploration and seismic research. FWI is an iterative algorithm that consists of two parts, forward modeling and inversion, where forward modeling generates simulated waveforms, and inversion updates model parameters by minimizing the difference between the actual waveform and the forward modeling waveform. FWI considers higher-order diffraction and scattering in the numerical solution, so it can capture more of the guided wave scattering physics, allowing it to capture more of the physics of guided wave scattering, and FWI can provide inversion results as precise as HARBUT [36].

Geophysicists first applied FWI to the fields of seismic exploration, oil and gas exploration, and geological structure exploration. Similar to geophysical exploration, non-destructive testing also estimates the internal structure and parameter distribution

of the measured tissue by observing the pressure field of the measured tissue and other information, and these two applications from different fields are based on the theory of wave mechanics. Therefore, the FWI method is expected to be applied in the field of guided wave tomography. The research in this paper is based on the FWI method.

As early as the 1980s, A. Tarantola [37-39] established a theoretical framework for time-domain FWI (both forward and inversion processes are implemented in the time domain), which is achieved by fitting actual measured data and estimated data to invert parameters. O. Gauthier et al. (1986) [40] and P. Mora et al. (1987) [41] realized the application of 2D FWI to real data. This study verified the ability of FWI to invert fine detail of structure, However, a serious shortcoming of the FWI method was also found, that is, the FWI method relies heavily on the initial model. In 1995, C. Bunks [42] first proposed the time-domain multi-scale FWI method, which effectively solved the strong nonlinearity of FWI by referring to the conventional idea of sub-step and sub-scale. In the 1990s, R.G. Pratt proposed the frequency domain FWI method [43] (both forward and inversion processes are implemented in the frequency domain), which uses several discrete frequencies to reconstruct high-precision images to save a lot of memory space. In 2004, L. Sirgue proposed a hybrid domain inversion method [44] (forward in the time domain and inversion in the frequency domain). The Laplacian domain FWI method proposed by C. Shin et al. [45] in 2008, Y. Cho et al. studied the Laplacian domain-frequency domain FWI method [46]; since 2011, E. Bozdağ, [47] studied the envelope-based FWI method.

An FWI-based ultrasonic guided wave tomography algorithm was first developed by J. Rao et al. [48] using A0 mode for corrosion mapping. Compared to linear scattering-based tomography methods, this method achieves higher reconstruction resolution by capturing higher order diffraction and scattering. This method, however, uses a lot of time and memory due to the vast quantity of calculation of the Jacobian matrix and the Hessian matrix. The low-frequency to high-frequency inversion approach is used to avoid the phenomenon of cycle skipping and local minima, which also takes time. There are also some prerequisites for a precise initial speed model as initial model.

The data-driven algorithm approach, which differs from the previous algorithms, utilizes deep learning or machine learning to learn the descent direction of an object function. For example, the Fast Inversion Tomography (FIT) algorithm created by M. Lin et al. [49] In this algorithm the Supervised Descent Method adopted to pre-learned the descent direction which avoided the massive calculation of Jacobian and Hessian matrices, and the global optimization algorithm of deep learning also avoided the danger of falling into a local minimum due to the cycle jump effect to a certain extent. However, the pre-training-based solutions also have certain limitations, such as the huge size of descent direction matrices, and the existing datasets are basically generated by simulation software, so it is never possible to find a real collected dataset that includes all kinds of defects and all material properties, there is still a certain gap between the simulated dataset and the actual acquisition waveform as well.

1.3 Main content of the thesis

This thesis is mainly divided into three parts. Conventional FWI, RNN-FWI, and experiment and result analysis.

In this study, we propose an ultrasonic guided wave tomography algorithm called RNN-FWI for corrosion inspection of plate using A0 mode. The recurrent neural network incorporates as basic framework in FWI. RNN-FWI consists of two stages: forward modeling and inversion, which is familiar with the conventional FWI. The forward modeling is computed sequentially by solving an acoustic wave equation with PML in the cyclic calculation unit of RNN. And the inversion is iteratively minimized a waveform misfit objective function of quadratic Wasserstein distance between forward modeling data and measured data. The gradient of objective function and model parameters are processed by automatic differentiation and the Adam algorithm, respectively. The velocity model generated in each iteration is regularized and parameterized by the U-Net DIP. Compared with the conventional FWI, the proposed method is not only superior to the traditional algorithm in calculation speed, efficiency and convergence speed, but also has good robustness and higher accuracy in the presence of noise. Moreover, the requirements for the initial model are lower than

formal one does, which breaks through the limitation of the classical FWI half-wavelength criterion and effectively alleviates the cycle skipping problem.

Finally, we design experiments to demonstrate the equivalence of RNN-FWI and conventional FWI, and demonstrate that gradient computation using automatic differentiation reduces systematic errors. Through experiments with different number of sensors, different optimization algorithms and different regularization methods, it is proved that RNN-FWI using Adam optimization algorithm, depth image prior regularization tool, and automatic differential gradient calculation tool has obvious improvement over conventional FWI.

1.4 Chapter arrangement of the thesis

This thesis studies the process from conventional FWI to RNN-FWI. This thesis consists of five chapters, and contents are arranged as follows.

In the first chapter, the background and significance of the research are introduced. Ultrasound as a nondestructive testing method, some methods of guided wave tomography and the development process of full waveform inversion are studied

The second chapter begins with the basic theory of Lamb wave, calculated the dispersion curve, provides a theoretical basis for subsequent full waveform inversion. Theory of conventional FWI including the forward modeling as well as the inversion method are studied, significant disadvantages and advantages are also presented at the same time, at last, the validation experiment and performance experiment of FWI algorithm are proposed.

In the third chapter, conventional FWI elaborate the theoretical implementation of RNN-FWI. The structure of RNN, some optimization algorithms of deep learning, the quadratic Wasserstein distance， two regularization methods based on CNN, and formula derivation of automatic differentiation are also introduced. At the same time, the validation experiment and performance experiment of RNN-FWI algorithm are finally proposed, which proves that RNN-FWI performance is better than conventional FWI to a certain extent.

In the fourth chapter, actual experiment setup and data processing are presented. This chapter mainly introduces the experiment performance of RNN-FWI in the actual experiment. Comparative experiments with different experimental variables (different parts relative to the conventional algorithm) demonstrate that the deep learning-based optimization method improves the overall performance of FWI.

In the fifth chapter, the summary and prospect of this thesis. The discussion of the advantages and limitations of RNN-FWI is followed in this chapter.

Chapter 2 Lamb Wave Principle and Conventional FWI

2.1 Introduction

When Lamb waves propagate in a plate-like structure, they are quite sensitive to the change of the plate in the thickness direction. Therefore, it is widely used in non-destructive testing. The attenuation of Lamb waves along the propagation direction is small and the propagation distance is long. Therefore, understanding the basic principles and propagation characteristics of lamb waves is the premise of effectively applying lamb wave nondestructive testing technology, and designing a specific lamb wave imaging detection scheme according to the imaging algorithm.

FWI is an iterative optimization method that produces high-resolution defect models, which is the estimation of model parameters by fitting modeled data to observed data. Modeling data is computed by solving the acoustic wave equation. Therefore, the application of FWI to lamb wave tomography can be very good for corrosion imaging of plate materials. Finally, this chapter conducts a series of simulation experiments on conventional FWI.

2.2 Principle of ultrasonic transmission in plate material

A wave is the propagation of vibrations in a medium. When the vibration direction of the medium particle is parallel to the advancing direction of the medium vibration wave, it is a longitudinal wave, when the medium particle vibration direction is perpendicular to the advancing direction of the medium vibration wave, it is a transverse wave, the waves generated by the mutual interference of longitudinal waves and transverse waves are surface waves. Compared with longitudinal waves and transverse waves, surface waves have the characteristics of slow attenuation and long-distance propagation. Surface waves can be divided into Rayleigh waves and Love waves.

Lamb wave is a new type of wave generated by the mutual reflection and coupling of the upper and lower surfaces of the plate during the propagation of transverse and longitudinal waves. It is a type of Rayleigh wave, when the thickness of the plate is in the same order of magnitude as the wavelength, not only the surface particles vibrate but the entire thin plate vibrates. During the propagation of lamb wave, the vibration displacement of medium particles can be decomposed into two directions along the direction of wave propagation and perpendicular to the direction of wave propagation, so the vibration of particles can be decomposed into horizontal and vertical components. According to the type of particle vibration, lamb waves can be divided into symmetric mode (S) and anti-symmetric mode (A) [1], as shown in Figure 2.1. The propagation speed of different modes in the plate is different, which is related to the thickness of the thin plate, the center frequency of the ultrasonic wave, and the properties of the material.

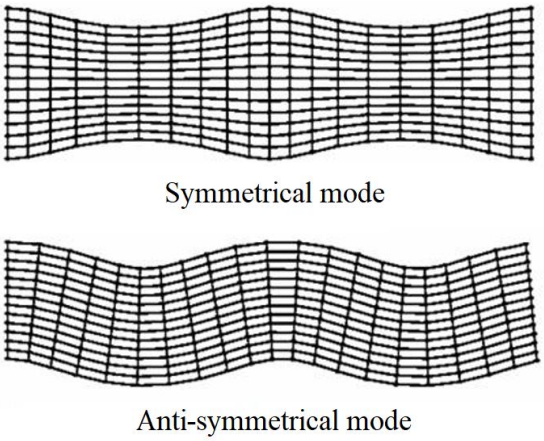

Figure 2.1 Symmetric and antisymmetric modes of lamb wave propagation

It is precisely because of the many advantages of lamb wave detection that lamb wave detection technology is expected to be widely used in the rapid and large-area detection of plate-like structures. However, due to the complexity of lamb waves in excitation mode, propagation characteristics, mode selection and defect wave signal processing, its wide application in industrial production is limited. These are all due to the multi-mode and dispersion characteristics of lamb wave propagation.

2.3 Dispersion characteristic curve of lamb

In infinitely large thin isotropic plates, the plate thickness is 2h, and h is close to the order of magnitude of the ultrasonic wavelength. It is assumed that the upper and lower interfaces of the board are free. There are two guided wave modes: symmetric and antisymmetric. The Rayleigh-Lamb frequency formula can be expressed as

Symmetric Mode:

$$\frac{\tan(Qh)}{\tan(Ph)} = -\frac{4k^2PQ}{\left(Q^2-k^2\right)^2} \tag{2.1}$$

Anti-symmetric mode:

$$\frac{\tan(Qh)}{\tan(Ph)} = -\frac{\left(Q^2-k^2\right)^2}{4k^2PQ} \tag{2.2}$$

Where,

$$P=\sqrt{\frac{\omega^2}{c_L^2}-k^2}\ ,\ \ Q=\sqrt{\frac{\omega^2}{c_T^2}-k^2}\ ,\ \ k=\frac{2\pi f}{c_p}$$

Formula 2.1 and 2.2 are for the symmetric and anti-symmetric modes, respectively, k is the wave number, c_p is the phase velocity of the Lamb wave, c_L is the longitudinal wave velocity, c_T is the shear wave velocity, and d is the thickness of the plate. The group velocity c_g and wavenumber k are related to the phase velocity c_p as follows:

$$c_g = {c_p}^2\left[c_p - fh\frac{dc_p}{dfh}\right]-1 \tag{2.3}$$

Finally, the graphical method [50] is used to acquire the numerical solution of dispersion formula of lamb wave, and the relationship between c_g and fh can be obtained, which is the dispersion characteristic curve of lamb and abbreviate as function $c_g=\psi(fh)$. The specific dispersion characteristic curve solving method is not the focus of this paper. The figure below shows the dispersion characteristic curve of the experimental aluminum plate. The specific parameters of the material will be introduced later.

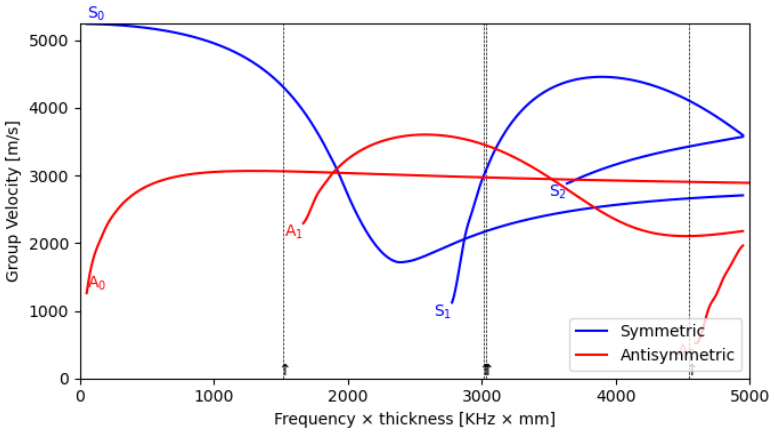

Figure 2.2 Velocity dispersion curves for an aluminum plate

According to this curve, the velocity map obtained by the tomography algorithm can be converted into a thickness map.

2.4 Lamb wave detection principle

Generally, ultrasonic transducers are coupled to the surface of the plate to act as drivers and sensors. The electrical excitation signal is generated by the signal generator, and then the electrical excitation signal is converted into an ultrasonic signal through the inverse piezoelectric effect of the piezoelectric wafer at the bottom of the transducer, and then enters the measured thin plate through the couplant, due to the constraint of the free boundary of the thin plate, the Lamb wave is already existed in the plate after propagating some length. Finally, the ultrasonic signal is converted into an electrical signal by receiving the positive piezoelectric effect of the piezoelectric chip at the bottom of the transducer for further analysis. When the Lamb wave propagates in the plate, if it encounters a significant distortion in the plate structure, such as delamination, holes and other defects, reflection and scattering phenomena will occur, which will make the wave packet amplitude and frequency components of the received response signal. and patterns may change. At this time, the defect information in the matrix tissue will be included in the response signal. By collecting the response signal, analyzing and extracting the defect information contained in it, the existence, shape and position of the defect can be discriminated. Finally, the non-destructive testing of materials and the evaluation of remaining life are realized.

2.5 Conventional full waveform inversion

2.5.1 Full waveform inversion as tomography

FWI avoids the ray assumptions used in TT (Travel Time), and higher order diffraction and scattering are automatically considered in FWI to improve resolution compared to DT (Diffraction Tomography) limited by linear scattering. In the FWI method, the forward model can be performed in the time or frequency domain. Time-domain FWI can be used to reduce the amount of computation.The remaining thickness and speed map can be easily evaluated with the dispersion curves from the previous subsection without adding extra cost to the formula.

It's worth noting that our studies were conducted on a flat isotropic plate with a center defect surrounding by a ring-shaped transducers array, in which every single transducer generate ultrasonic waves in sequence and in the meanwhile all the other transducers receive waveforms. The following figure is a schematic diagram of the experimental setup. Forward modeling of FWI is the process of numerically propagating a wave source in the model and recording the wave field at the receive transductor location. The FWI can be performed in time or frequency domain, in contrast to frequency domain, time domain covering the whole frequency spectrum, provides a precise solution, and it’s easy to window the wanted signals. The specific algorithm process will be described in detail next subsection.

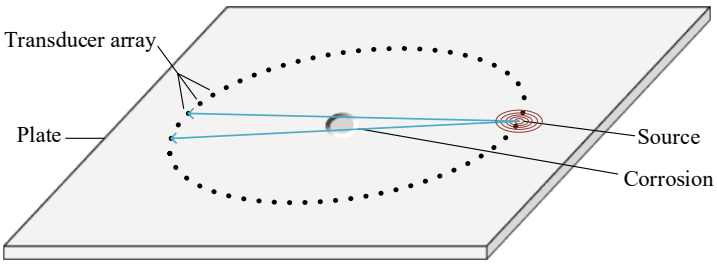

Figure 2.3 Experimental setup of lamb tomography

2.5.2 FWI algorithm detail

The 2D acoustic wave formula in constant density medium can be expressed as [48]:

$$\left(\frac{1}{v^2(r)}\frac{\partial^2}{\partial t^2}-\nabla^2\right)p(r,t)=s(r,t) \tag{2.4}$$

$$p_t=\xi(s_t) \tag{2.5}$$

where $p(r,t)$ is the pressure wavefield, $s(r,t)$ being the source, r being the 2-D or 3-D space vector, t being the time variable, $v(r)$ being the guided wave speed, ∇^2 being the spatial Laplacian operator, and ξ represents the forward operator. A common method for solving differential formulas is to first discretize the space-time coordinates of the problem and complete the solution in the form of numerical integration. Formula 2.4 can be calculated and discretized using the finite difference method, and the wave field can be calculated at the finite difference grid points. It should be noted that forward modeling in FWI generally employs the finite difference and finite element methods, but the finite difference method outperforms the finite element method in terms of calculation speed and memory consumption. Calculating the realistic physical model in three-dimensional is not suitable for iteration algorithm because of inefficiency and complexity.

According to the Mindlin plate theory [51], which provided an approximation model of A0 mode guided wave with dispersive properties by neglecting thickness of plate-like materials. In this way, complexity of calculating was greatly reduced, speeds up computing speed, and enables various optimization algorithms to run efficiently within a reasonable loss range. The second-order finite difference defined as

$$\frac{\partial^2 p(r,t)}{\partial t^2}=\frac{1}{\Delta t^2}\left[p(r,t+1)-2p(r,t)+p(r,t-1)\right] \tag{2.6}$$

where Δt is time step. Bring formula 2.4 into formula 2.6, and after calculation, the following can be obtained

$$p(r,t)=v^2(r)\Delta t^2\left[\nabla^2 p(r,t-1)+s(r,t-1)\right]+2p(r,t-1)-p(r,t-2) \tag{2.7}$$

The above is the forward formula of FWI. In this way, the value of the wave field at all times can be obtained by explicitly calculating formula 2.7, the waveform transductors responsible for receiving can be obtained as well. The Perfectly Matched Layer (PML) [52] is an accurate and reliable solution for decreasing reflections.

The objective function or cost function of the conventional Full Waveform Inversion is the sum of the $L2$ distance between the simulated wave field value and the observed wave on all receiving transductors, described like

$$\arg\min C(m)=\frac{1}{2}\sum_{i=1}^{N_S}\sum_{j=1}^{N_R}\left\| p_{i,j}^{sim}(m)-p_{i,j}^{obs}\right\|_2^2 \tag{2.8}$$

where m is $1/v^2(r)$, $N_S N_R$ are number of transmitting and receiving transductors, p^{sim} and p^{obs} is simulated wave and observed wave.

The inversion step of Full Waveform Inversion often relies on a conventional solution of ordinary differential formula derivation called the adjoint state method, this calculation method is similar to reverse time migration. Reverse time migration uses the zero-delay cross-correlation calculation of the forward wave field and the reverse wave field, and the source of the reverse wave field is the waveform of the forward wave field. If the source of the backpropagating wave field is changed to the difference between the observation record and the simulated record, that is, the residual record, this process becomes the gradient calculation process by the adjoint state method. The result is as follows [53-54]:

$$\nabla C(m)=-\frac{2}{v^3}\sum_{t=1}^{N_t}\frac{\partial^2 p_{t-1}}{\partial t^2}\xi^{-1}\left(p^{sim}-p^{obs}\right) \tag{2.9}$$

Using the adjoint state method can avoid a lot of unnecessary trouble caused by directly calculating the gradient [55], for example, if the Gauss-Newton method [56] is used to compute the gradient directly, the objective function is approximated by a second-order Taylor expansion

$$C(m_0+\Delta m)=C(m_0)+\frac{\partial C(m_0)}{\partial m}\Delta m+\frac{1}{2}\Delta m^T\frac{\partial^2 C(m_0)}{\partial m^2}\Delta m+O\left(m^3\right) \tag{2.10}$$

where Δm represents the model parameter perturbation， $O\left(m^3\right)$ is higher order error term which seems as zero usually, the derivative of the objective function with respect to the model parameter m as

$$\frac{\partial C(m)}{\partial m}=\frac{\partial C(m_0)}{\partial m}+\frac{\partial^2 C(m_0)}{\partial m^2}\Delta m \tag{2.11}$$

To minimize the objective function in the neighborhood of m_0, the value of formula 2.9 must be zero. The gradient can be computed directly by taking the derivative of formula 2.12:

$$g = \nabla C(m) = \frac{\partial C(m)}{\partial m} = \sum_{i=1}^{N_S}\sum_{j=1}^{N_R} J_{i,j}^{\dagger}\left(p_{i,j}^{sim}(m) - p_{i,j}^{obs}\right) \tag{2.12}$$

where $J_{i,j}^{\dagger}$ is adjoint of Jacobian or Fréchet derivative matrix which write as $\frac{\partial p^{sim}(m)}{\partial m}$ represents the partial derivatives of the forward modeling data at the receiving point to the model parameters at each grid point of the entire model, g represents the gradient descent direction

Then use the second-order optimization algorithm such as the L-BFGS-B method [57] to update the parameters of the model, iteration step size calculation involves Hessian matrix or approximation Hessian matrix. The model parameter is updated iteratively according to

$$m^{(k+1)} = m^{(k)} - a^{(k)} g'^{(k)} \tag{2.13}$$

Where a is step length, and k is step number of iterations, g' is the gradient with regularization which provide calculation stability, in order to provide stable and reliable results, we apply some regularization to the gradient, total-variation (TV) [58] or Tikhonov is one of the most popular regularization techniques in FWI algorithm, TV is a non-quadratic regularization method that imposes sharp edges without over-smoothing the reconstructed the model.

$$g' = g + \lambda_{TV} g_{TV} \tag{2.14}$$

$$g_{TV} = \arg\min\left|\left(\frac{\partial m}{\partial x}\right)^2 + \left(\frac{\partial m}{\partial y}\right)^2 + \varepsilon_{TV}\right| \tag{2.15}$$

Where the regularization coefficient λ_{TV} implies the confidence level between the terms involved in the functional, ε_{TV} is a smoothing parameter.

In formula 2.13, a is speed map update step length, which is calculated by the optimizer algorithm. The commonly used optimization algorithms are conjugate gradient method, Newton method, quasi-Newton method and so on. Compared with ordinary Newton's method, L-BFGS-B inherits the advantages of fast convergence speed and saves calculation. However, when L-BFGS-B calculates the gradient, it needs to use all the data for calculation. The principle of L-BFGS-B algorithm is shown in Table 2.1.

Table 2.1 Principle of L-BFGS-B algorithm:

$p^{(k)} = x^{(k+1)} - x^{(k)}$, $q^{(k)} = \nabla f\left(x^{(k+1)}\right) - \nabla f\left(x^{(k)}\right)$

Quasi-Newtonian condition: $p^{(k)} = H_{k+1} q^{(k)}$,where H_{k+1} is approximate matrix of the inverse of the Hessian matrix

BFGS formula:

$$H_{k+1} = H_k + \left(1 + \frac{q^{(k)T} H_k q^{(k)}}{p^{(k)T} q^{(k)}}\right) \frac{p^{(k)} p^{(k)T}}{p^{(k)T} q^{(k)}} - \frac{p^{(k)} p^{(k)T} H_k + H_k q^{(k)} p^{(k)T}}{p^{(k)T} q^{(k)}}$$

L-BFGS-B formula:

$$\begin{aligned} H_{k+1} = {} & v_k^T v_{k-1}^T \cdots v_{k-m+1}^T H_0 v_{k-m+1} \cdots v_{k-1} v_k \\ & + v_k^T \cdots v_{k-m+2}^T \beta_{k-m+1} p_{k-m+1} p_{k-m+1}^T v_{k-m+2} \cdots v_k \\ & \cdots \\ & + v_k^T \beta_{k-1} p_{k-1} p_{k-1}^T v_k + \beta_k p_k p_k^T \end{aligned}$$

Where $\beta_k = 1 / p_k^T q_k, v_k = (1 - \beta_k q_k p_k)$

L-BFGS-B iteration formula:

$$x^{(k+1)} = x^{(k)} - H_{k+1} \nabla f\left(x^{(k)}\right)$$

The calculation is completed when the objective function is lower than the predetermined threshold

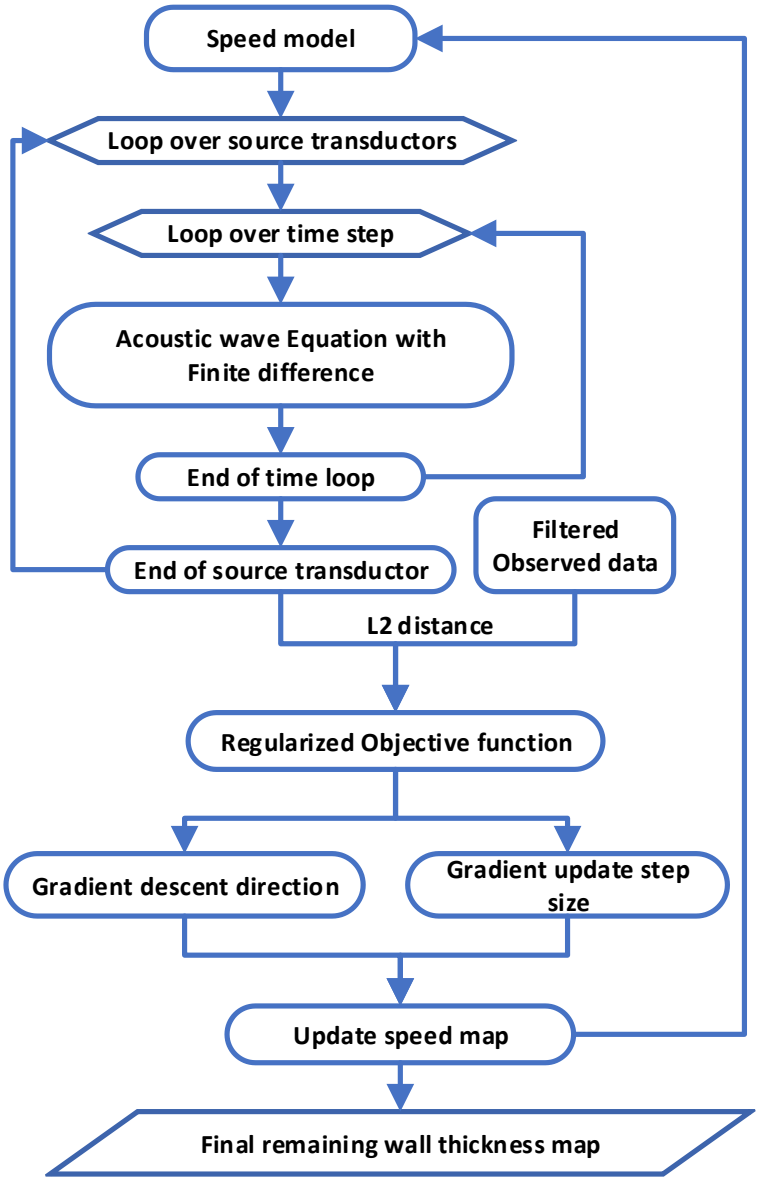

Figure 2.4 Structure of the conventional FWI algorithm.

Figure 2.4 depicts the steps of conventional FWI.

Although FWI is one of the most accurate reconstruction approaches, it has numerous disadvantages. To begin with, computation of Jacobian and Hessian matrices for gradient calculation and local optimization techniques (such as L-BFGS-B) in conventional FWI is time-consuming. Furthermore, the whole waveform data is involved in Newton algorithms for calculation, so the memory requirements are likewise very large. In reality, the objective function is the least square difference L2 between the simulated and real data, when the initial velocity model is inaccurate or the defect is too deep, the half-wavelength criterion will not be satisfied, that is, the

waveform difference exceeds half a wavelength distance, a cycle jump phenomenon will occur. For the TV regularization term of conventional FWI, the effect of regularization depends on the hyperparameters, which inefficiently consumes a lot of trial-and-error experiments to determine. TV regularization has the effect of maintaining the sharp edges of the model while Tikhonov regularization is prone to over-smoothing, however, the shape of real corrosion defects is generally complex, traditional regularization methods have certain limitations, which limit the accuracy of reconstruction. Moreover, most integrators in the adjoint state method cannot guarantee strict time-reversal symmetry [60], so the adjoint state method often has systematic errors related to the integration step size.

2.6 Experiment with conventional FWI

2.6.1 Numerical simulation setup

This section is about the numerical simulation experiment of full waveform inversion. The experimental material is a 1000*1000*10mm aluminum material with the label of 6061, which is consistent with our subsequent real experiments. A 100mm PML layer is used to absorb boundary echoes. The density of the material is 2.9g/cm3, the Young's modulus is E=71Gpa, the Poisson's ratio is 0.33, and the size of the finite difference mesh is 2mm, guaranteed to be four times less than the Lamb wave wavelength (λ≈30mm), and the time step is $5.0*10^{-7}s$. we use a 60-point circular array with a diameter of 700mm records and emits lamb waves, and the corrosion defects consist of depressions of different shapes in the very center of the plate, with a maximum depth of half the thickness. As shown in Figure 2.5, in the experiment, we applied the excitation of displacement perpendicular to the plate surface at one of the transductor positions in sequence (red dot is excitation place, while green dots are receiver places). The excitation function is a Hanning windowed five-period sine wave toneburst signal, the center frequency is 50KHz, and the 15db bandwidth is 35- 65KHz, is shown in Figure 2.6 below

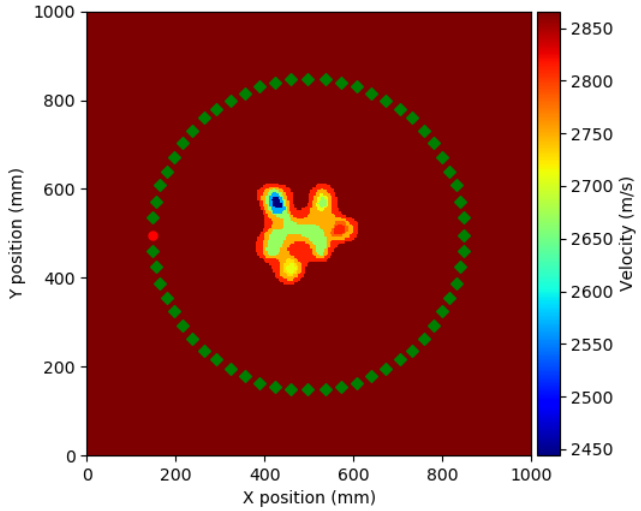

Figure 2.5 Simulation experiment setup.

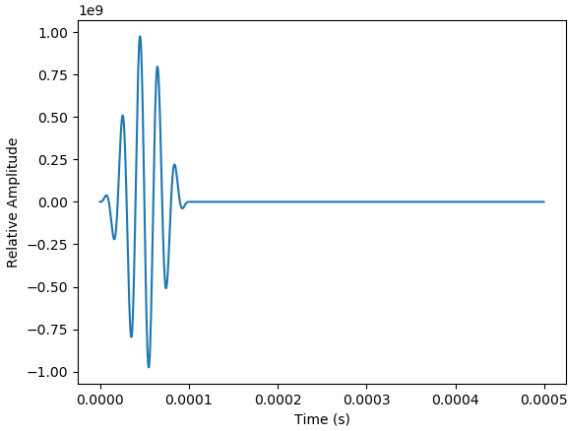

Figure 2.6 Excitation function is a five-period sine wave of Hanning window.

Applying a normal force perpendicular to the plate surface at 50KHz can ensure the excitation of pure A_0 mode Lamb waves, although the S_0 mode exists, it is very weak and negligible relative to A_0 mode. It can be seen from Figure 2.2 that within $0.5Mhz \cdot mm$ the dispersion curve is sensitive to thickness variation without interference from other guided wave modes.

2.6.2 Numerical simulation results

(1) Absolute wavefield map

Figure 2.7 shows the absolute value of the difference between the wavefields received by all receivers without defects and with defects, gradient information is

contained in it, so that optimizer can use this map to calculate gradient.

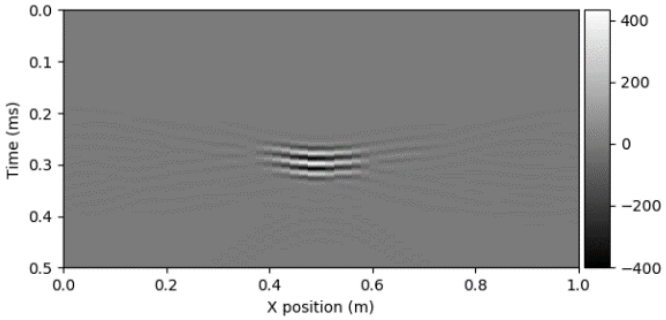

Figure 2.7 Absolute map of wave field.

(2) 1D reconstruction result by FWI

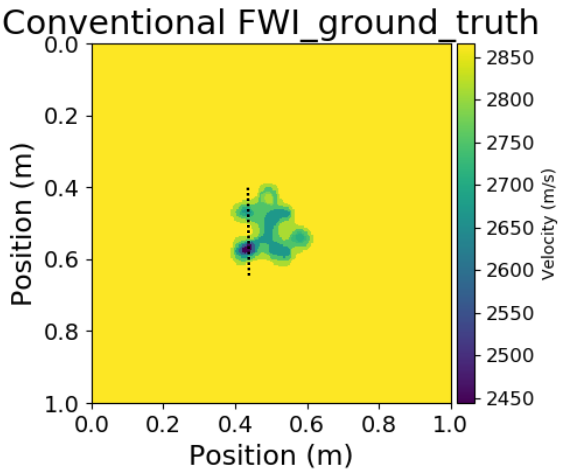

Figure 2.8 Position of profile.

We extracted 1-dimensional corrosion model information for inversion from the dotted line position in Figure 2.8 as a cross section. Among them, there are 9 sensors, evenly distributed on the surface of the 1D model. They can both transmit and receive. During the experiment, the sensors transmit in turn, and other sensors receive. The experiment simulated the scene of one side not corroded and the other side corroded.

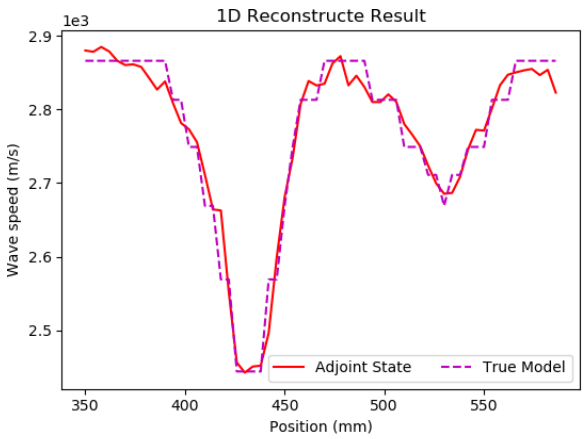

Figure 2.9 Reconstruction of 1D model using FWI.

The experimental results are shown in the figure above. The inversion basically matches the shape of the defect, and the corrosion is reconstructed in good condition both from slope and edge. However, it is worth mentioning that such a dense sensor is not desirable in real industrial applications. This experiment only proves the high precision performance and feasibility of FWI in the reconstruction of speed model.

(3) 2D reconstruction result by FWI

Next, we will use the same corrosion model as in the section of experimental setting. In order to visually show the difference between the inversion result and the real damage, we extract the velocity map profile at the position of the black line in the figure 2.8. All data will be performed with 8 epochs, and the optimizer uses L-BFGS-B algorithm.

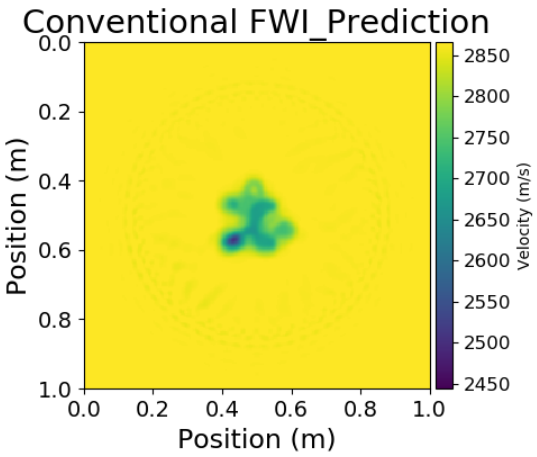

Figure 2.10 The inversion results.

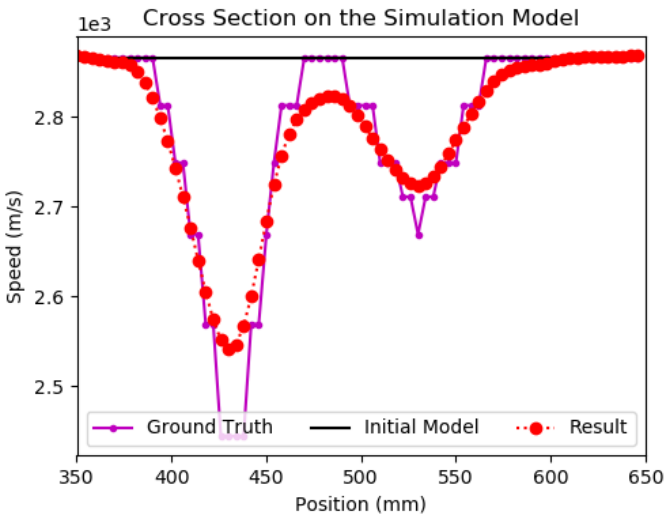

Figure 2.11 Position of profile.

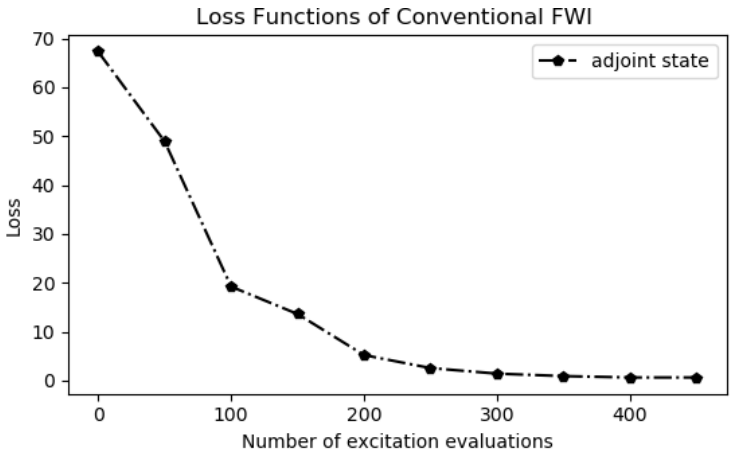

Figure 2.12 Loss functions of FWI.

It can be found that the conventional FWI has performed a good inversion of the contour and depth of corrosion, and no obvious artifacts appear in the numerical simulation experiment without noise and waveform deformation. The slope near the contour is very similar to the actual corrosion. For depth inversion, the depth of the deep pit is not good. In terms of calculation time, the convergence curve (loss curve) is shown in the figure, and the loss stabilizes after 300 iterations, proving that 5 epochs is sufficient for this model. FWI took about 15 minutes to complete convergence

Next, we set up a ladder descending corrosion model. It is worth noting that this model is not as complex as the previous model and the corrosion trend is relatively simple. The rest of the experimental setup is the same as the first one. The location of the profile of the velocity diagram is shown in below (Dotted line).

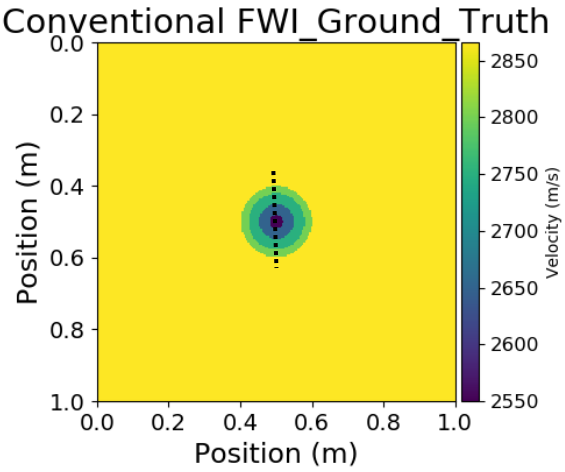

Figure 2.13 Corrosion model of ladder descent and profile location.

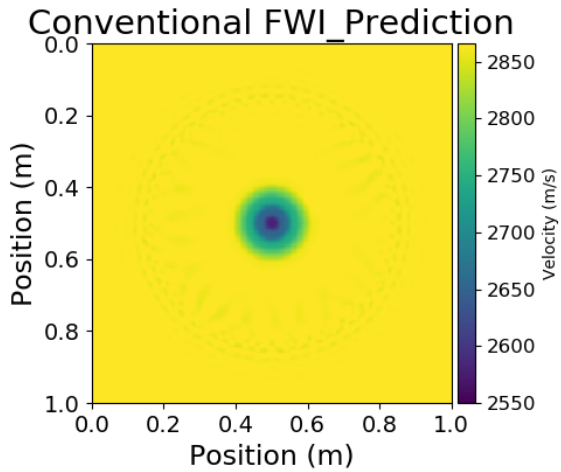

Figure 2.14 The inversion results.

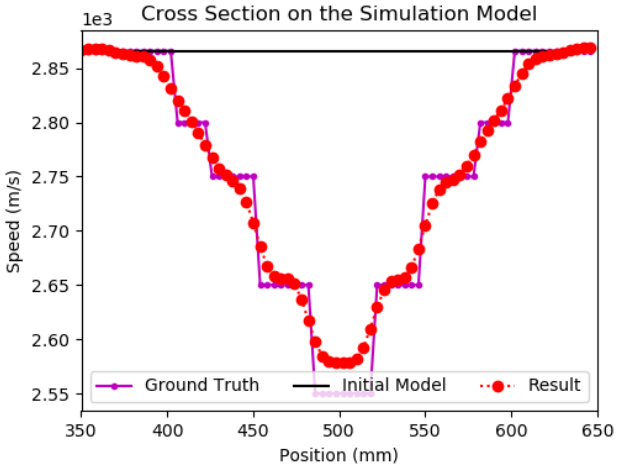

Figure 2.15 Position of profile

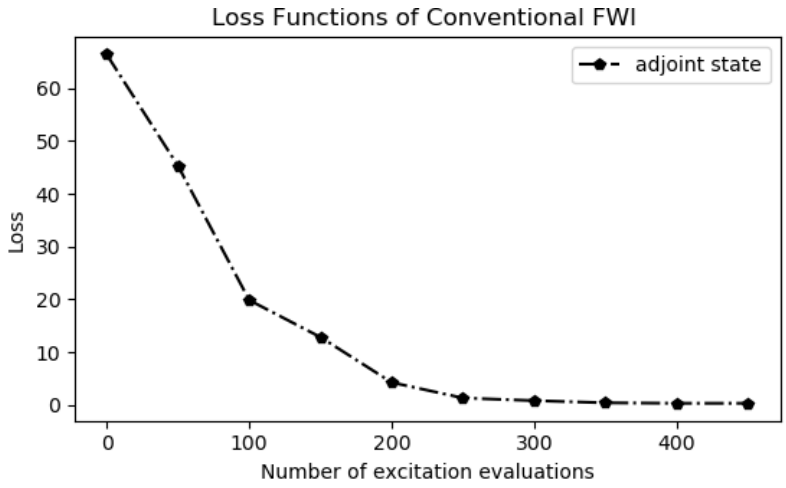

Figure 2.16 Loss functions of FWI.

For the defect with relatively single trend, FWI reconstruction reflects the slope well, and the inversion of depth is also considerable. Convergence can be achieved after 4 epochs. The inversion also took 15 minutes.

2.7 Conclusion

To apply lamb wave for imaging detection, it is necessary to master the basic principles and characteristics of lamb waves. This chapter firstly introduces the ultrasonic wave in plate material and the basic theory and propagation characteristics of lamb wave propagation are also introduced. Based on the equation of lamb wave, its multi-mode characteristics and dispersion characteristics during propagation are analyzed. The dispersion curve is the basis of the imaging detection method in the following text, the imaging detection method based on lamb wave is introduced

Finally, a high-precision lamb tomography algorithm for defect inversion, also known as FWI, is introduced. After introducing the structure and advantages and disadvantages of the algorithm, we use this new but conventional algorithm for numerical simulation and draw conclusions.

Chapter 3 RNN-FWI for Guided Wave Tomography

3.1 Introduction

FWI consists of the forward propagation of the wave field and the back propagation of the residual, this process is very similar to the Back Propagation (BP) algorithm in the artificial neural network, BP is also fed forward first, and then the error is back propagated. Both algorithms are calculating gradients and updating parameters iteratively. Therefore, FWI and deep learning neural networks are very similar, we can try to introduce FWI into deep learning, so that the various optimization techniques and advantages of deep learning can further improve the performance of conventional FWI.

In this section we introduce the theoretical fundamentals RNN-FWI, which the conventional Full Waveform Inversion is the fundamental of RNN-FWI.

3.2 RNN-FWI

3.2.1 Recurrent neural networks as architecture of FWI

Recurrent Neural Networks are a class of artificial neural networks in which layers are connected by a sequence of directed graphs. RNNs use their internal state (memory) to process input sequences, which makes them suitable for time sequence signal processing tasks such as handwriting recognition and speech recognition. Re-observing the formula 2.7, due to the time directionality of wave propagation, that is, the wave field at the current time is only affected by the wave field in the past two time periods and not by its future state, so the directed acyclic graph RNN is suitable for wave simulation [59].

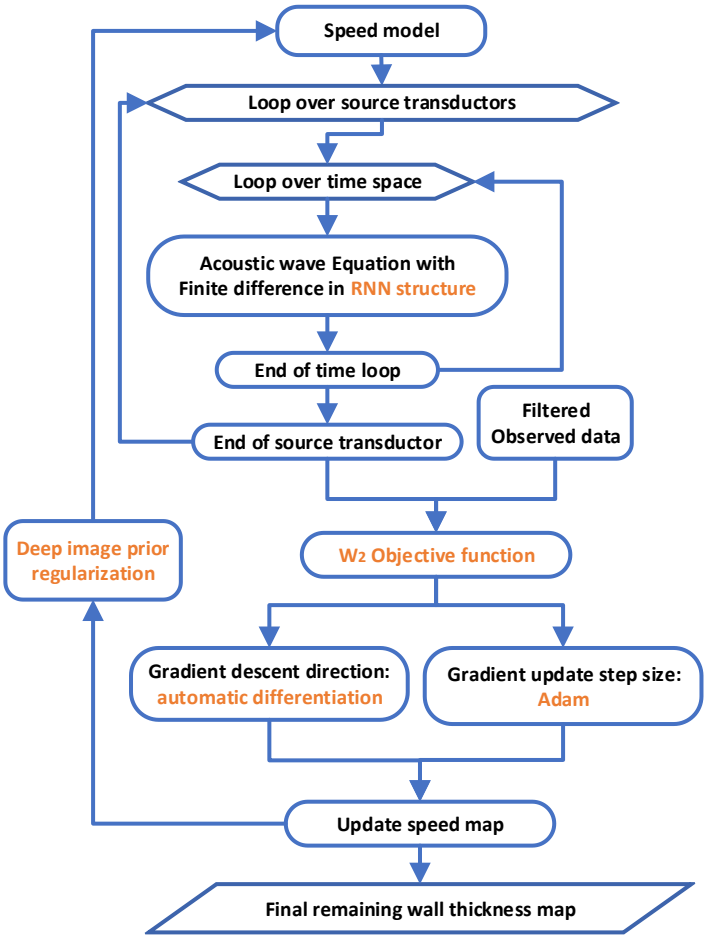

Figure 3.1 Workflow of the RNN-FWI algorithm.

We propose an FWI algorithm based on RNN. The structure of RNN-FWI is basically the same as the traditional one： the basic structure is shown in Figure 3.1, the sequence computation of the convolutional neural network is used to realize the time series forward modeling of the acoustic wave formula based on the finite difference method, the Adam algorithm and automatic differentiation method minimize the W2 distance between the simulated waveform and the observed waveform and update the speed map and the weight of DIP then generate the initial speed map for the next iteration.

The wave field at the current time is only determined by the wave field in the past two time periods, and does not depend on its future state. So, the directed acyclic graph RNN is suitable for realizing acoustic wave equation. This inspires the formulation of

the forward modeling problem in terms of a recurrent neural network, with each cell representing the wavefield at a single step in time.

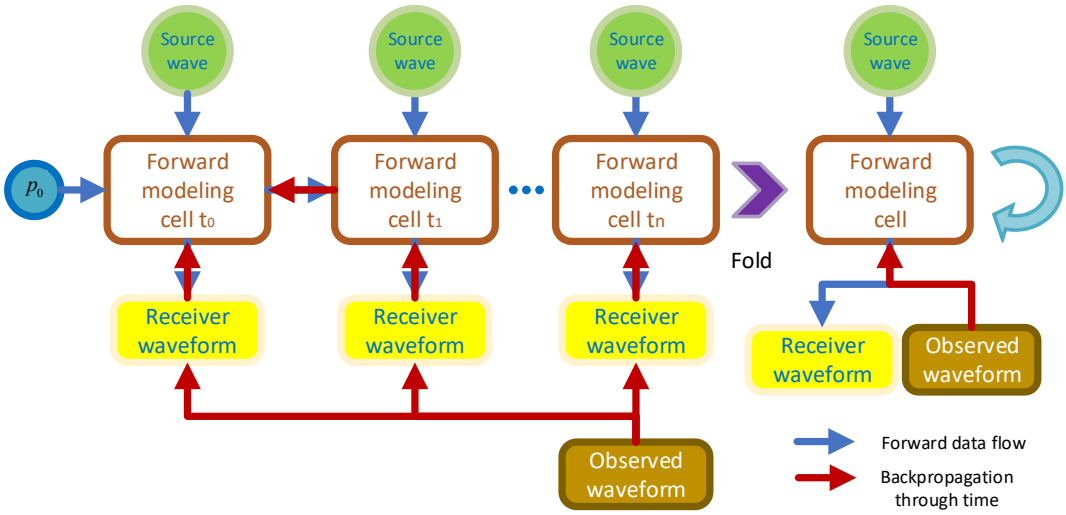

Figure 3.2 Structure of the unrolled RNN-FWI algorithm.

To build an RNN architecture supportive of acoustic wave modeling, forward modeling is achieved by repeatedly applying a series of arithmetic operations corresponding to one-time step of the finite difference acoustic wave equation in every cell. The data consists of state vectors and external inputs that are passed from one unit to the next and represent the current state of the system. In this case, the trainable variables are velocity model in acoustic wave equation, inputs are source waveform and each cell outputs the receiver waveform. Figure 3.2 is the schematic diagram of compact and unrolled form RNN. Blue arrows indicate the forward modeling and red arrows represent the inversion, which is consistent with convention FWI.

Figure 3.3 depicts the detailed cell architecture of an RNN capable of simulating guided wave propagation. Where the inputs wavefields and are two previous time steps, the source term at the current time step, is the auxiliary wavefield of the PML. The outputs and at and are waveforms at receiver locations and the wavefield at the current time and last cell memory, respectively. In Figure 3.3, all the arithmetical operations are corresponded to formula 2.7 including the PML calculation. Trainable parameters are included in the RNN graph to set up the network to accommodate velocity inversion,

as shown in the red box in Figure. Observed waveform data being the labeled data of the training set consists of the part of objective function.

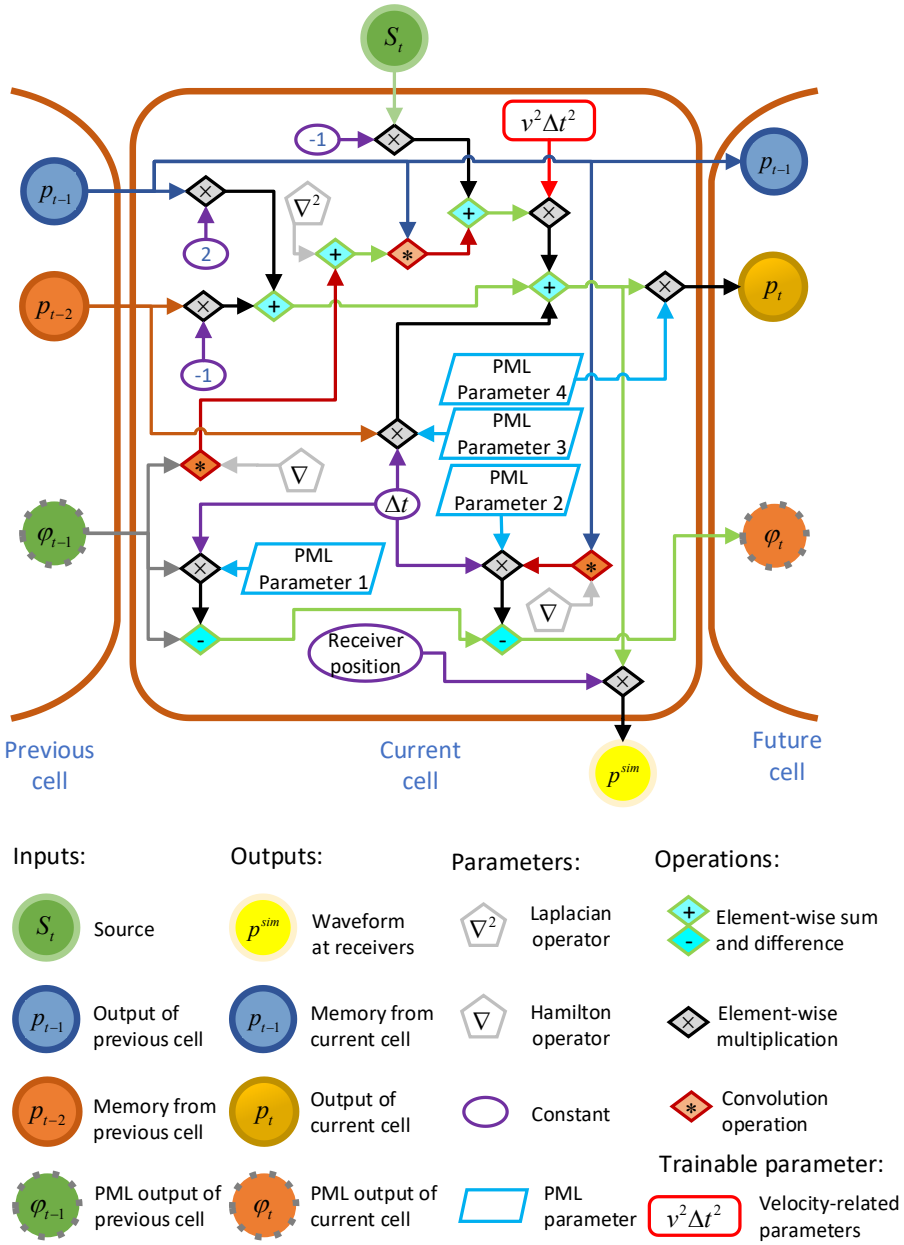

Figure 3.3 The single cell architecture of the RNN-FWI with PML.

The parameter update relies on the gradient calculation of the objective formula, and the automatic differentiation uses the accumulative chain rule to calculate the gradient of the loss function with respect to the wavefield at each time step and the

gradient of the wavefield with respect to the velocity speed model. The gradient of the loss function to the wavefield p_t for a time step is calculated as follows:

$$\left.\frac{\partial C}{\partial p_t}\right|_v = \left.\frac{\partial C}{\partial p_t}\right|_{v,p_{t'\neq t}} + \left.\frac{\partial C}{\partial p_{t+1}}\right|_v \left.\frac{\partial p_{t+1}}{\partial p_t}\right|_{v,p_{t'\neq t,t+1}} + \left.\frac{\partial C}{\partial p_{t+2}}\right|_v \left.\frac{\partial p_{t+2}}{\partial p_t}\right|_{v,p_{t'\neq t,t+2}} \tag{2.1}$$

The gradient of the wave field to the velocity graph is calculated using the chain rule:

$$\frac{\partial C}{\partial v} = \sum_{t=1}^{N_t} \left.\frac{\partial C}{\partial p_t}\right|_v \left.\frac{\partial p_t}{\partial v}\right|_{p_{t'\neq t}} \tag{2.2}$$

Take the partial derivative of first term of equation 3.1:

$$\left.\frac{\partial C}{\partial p_t}\right|_{v,p_{t'\neq t}} = p^{sim} - p^{obs} \tag{2.3}$$

Calculate each term of equation 3.1 by taking the partial derivative of each term of equation 2.7:

$$\left.\frac{\partial p_{t+1}}{\partial p_t}\right|_{v,p_{t'\neq t,t+1}} = \nabla^2 v^2 \Delta t^2 + 2 \tag{2.4}$$

$$\left.\frac{\partial p_{t+2}}{\partial p_t}\right|_{v,p_{t'\neq t,t+2}} = -1 \tag{2.5}$$

$$\left.\frac{\partial p_t}{\partial v}\right|_{\substack{p \\ t'\neq t}} = 2v\Delta t^2 \left(\nabla^2 p_{t-1} + s_{t-1}\right) \tag{2.6}$$

The gradient of the objective formula of the full waveform inversion calculated by automatic differentiation can be obtained by simplifying the above formulas, which is consistent with formula 2.9, the result of the adjoint state method.

$$\frac{\partial C}{\partial v} = \sum_{t=1}^{N_t} -\frac{2}{v^3} \frac{\partial^2 p_{t-1}}{\partial t^2} \zeta^{-1} \left(p^{sim} - p^{obs}\right) \tag{2.7}$$

In the iterative calculation, the adaptive moment (Adam) algorithm is used to optimize the parameter update. Compared with the conventional FWI using the Newton method or the quasi-Newton method, the Adam algorithm adopts the idea of small batch data processing, which not only has a fast convergence speed, but also does not require all data to participate. For calculation, the memory required is small, and the precision is high, which is a better convergence algorithm. Adam is a first-order optimization algorithm that can replace the conventional stochastic gradient descent process, which

iteratively updates neural network weights based on training data. The specific process is shown in Table 3.1.

Table 3.1 Principle of ADAM algorithm:

Parameter 1: Learning rate (step size) ε

Parameter 2: Exponential decay rate of moment estimates ρ_1 and ρ_2

Parameter 3: Small constant for numerical stabilization δ

Parameter 4: Maximum number of iterations T

Parameter 5: Initial Parameters θ

Initialize first and second moment variables $s_0 = 0, r_0 = 0$

Initialize time step $t = 0$

When $t < T$:

Calculate gradient: g_t

$t \leftarrow t + 1$

Update the biased first moment estimate: $s_t \leftarrow \rho_1 s_{t-1} + (1-\rho_1) g_t$

Update the biased second moment estimate: $r_t \leftarrow \rho_2 r_{t-1} + (1-\rho_2) g_t \otimes g_t$

Correcting the deviation of the first moment: $\hat{s}_t \leftarrow s_t / (1-\rho_1^t)$

Correcting the deviation of the second moment: $\hat{r}_t \leftarrow r_t / (1-\rho_2^t)$

Calculate update: $\Delta\theta_t = -\varepsilon \cdot \hat{s}_t / \left(\sqrt{\hat{r}_t + \delta}\right)$

Apply update: $\theta \leftarrow \theta + \Delta\theta_t$

In addition, the conjugate gradient method is a method between the steepest descent method and the Newton method. It only needs to use the first-order derivative information, but it overcomes the shortcoming of the slowest convergence of the steepest descent method, and avoids the need for storage and calculation of the Newton method. The disadvantage of the Hesse matrix and its inversion, the conjugate gradient method is not only one of the most useful methods for solving large linear formulas, but also one of the most efficient algorithms for solving large nonlinear optimization.

Therefore, we will horizontally compare the performance of RNN-FWI under L-BFGS-B, ADAM and conjugate gradient optimization in subsequent chapters.

In addition, ultrasonic waves can travel to "infinite" distances in all directions in the simulation, however, this is not feasible to solve the wave formula in a discrete infinite domain. To compensate, an auxiliary wavefield φ_t needs to be used to achieve Perfect Matching Layers (PML) to model infinite domains [61], which allow approximation of infinite size by damping and absorbing waves at the limit border of the domain to avoid reflections. This will make some corrections to the wave's propagation formula in each unit.

In addition, because of the optimization of convolution operations in the deep learning framework (TensorFlow), we can use convolution operations with finite difference kernels to speed up the computation of spatial derivatives in wave formula solutions while saving memory resources [63].

3.2.2 Quadratic Wasserstein distance as objective function

FWI is a nonlinear inversion algorithm, the highly nonlinear relationship will lead to local minimum in the Objective functional, which makes the inversion unable to converge to the correct result. The classic full waveform inversion method uses the least squares difference between the simulated data and the real data as a misfit function. When the initial model is inaccurate or the defect is too deep, the waveform difference between the simulated data and the real observation data exceeds half a wavelength. There will be a cycle jump phenomenon, which increases the probability that the model solution mismatch with the global optimal solution.

Wasserstein distance is a mathematical tool inspired by optimal transport theory that measures the difference between two distributions by the optimal cost of rearranging one distribution to another, the basic idea is to treat the comparison of two distributions as an optimal mapping problem. This solves an optimization problem to calculate the distance between two distributions. In the study presented by Engquist and Froese (2014) [65], the measurement of distance is not based on pure differences in oscillating signals, but on all the mappings that can move and distort the original signal

to map the target signal. Therefore, this distance can capture the information of the travel time offset and amplitude change of the signal.

Here we give the definition of the W2 distance. First, the waveform data is linearly transformed to a non-negative space: $S(p)=p+c$, normalizing the waveform distribution: $\tilde{p}(t)=\frac{S(p)(t)}{\int_0^{T_0} S(p)(t)dt}$, and then find its empirical distribution: $P(t)=\int_0^{T_0}\tilde{p}(\tau)d\tau$, the least squares distance of the inverse of the empirical distribution is the W2 distance:

$$W_2^2\left(\tilde{p}^{sim},\tilde{p}^{obs}\right)=\int_0^T\left|t-P^{obs^{-1}}(P^{sim}(t))\right|^2\tilde{p}^{sim}(t)dt \tag{17}$$

$$=\int_0^1\left|P^{sim^{-1}}(s)-P^{obs^{-1}}(s)\right|^2 ds \tag{18}$$

So, the objective function of full waveform inversion is rewritten as $\arg\min C(m)=\frac{1}{2}\sum_{i=1}^{N_S}\sum_{j=1}^{N_R}W_2^2\left(\tilde{p}_{i,j}^{sim}(m),\tilde{p}_{i,j}^{obs}\right)$. The quadratic Wasserstein metric inversion has less dependent on the initial model [66]. In the case where the initial guess is quite different from the real model, W2 avoids cycle skipping issues by both measuring waveform differences and global phase shifts, so the objective function has better convexity and is an effective means to reduce cycle skipping [67].

In addition, since the gradient of the target equation is calculated by automatic differentiation, there is no need to consider redefining the explicit differential equation, which brings certain convenience to the development.

3.2.3 Regularization method based on deep image priors

However, since the inverse problem is usually ill-conditioned and strongly nonlinear, which may trap the inversion into local minima, artifacts from the local minima can interfere with the imaging results, and the conventional solution is to use a mismatch function with a regularization term, such as objective formula with a user-defined regularization weight damping term or Tikhonov method and total variation regularization method. Ulyanov et al. (2018) [62] working on depth image priors showed that CNN architectures without pretraining can be used as priors which shows

significant effect in denoising and super-resolution, for neural networks with convolutional layers, local convolution kernels applied across the domain have self-similarity and spatial correlation. Therefore, reparametrizing the velocity speed model parameter with a convolutional neural network naturally introduces regularization to the FWI. We can represent the velocity model with a generative neural network, which can naturally introduce spatial correlation as a regularization into the generative velocity model, thereby suppressing noise in gradients and mitigating local minima, and significantly improving inversion in the presence of noise. Furthermore, not all image priors have to be learned from the data, instead, a large amount of image statistics is captured by the structure of the generator ConvNets, so no additional training data and optimization training loops are required for the deep image prior [64].

CNN-based deep image priors can functionally illustrate the regularization of FWI by deep convolutional networks, and in this way, we can use some more advanced deep network architectures to better extract the priori information in speed model at each iteration.

UNet+Resnet including skip connection layer was originally applied to medical image segmentation, and its structure is simple and can obtain features of different scales to a certain extent. According to the structure of UNet, it can combine low-level and high-level information, and the low-resolution information after multiple down-sampling can provide contextual information of defects message in the entire image, which can be understood as a feature that reflects the relationship between the corrosion priori information and speed map. After the concatenate operation, the high-resolution information is directly transmitted from the encoder to the decoder of the same height. The skip connections play the role of supplementary information, and the image details are supplemented at the high level to ensure that the features are more refined. UNet combines low-resolution information and high-resolution information, which not only works well in medical image segmentation, but also excels in many Image to Image tasks, and is perfectly suitable for deep image priors.

Therefore, we designed a DIP-UNet that uses UNet to achieve FWI regularization. The structure diagram is shown in Figure 3.4, and the parameter details of UNet are

detailed in Table 3.2. We directly combine the output of the neural network with the speed model updated by the RNN as the speed map parameter update for the next FWI loop, so a neural network is trained to predict updates to the speed model. Update to neural networks in NNFWI directly use gradients computed by automatic differentiation. The gradients are directly back-propagated from the loss through the partial differential equations and neural network layers to the weights of the neural network.

After calculating the final slowness map in the FWI, we can convert a velocity map to a thickness map by using the material's dispersion curve, which is the group velocity-frequency thickness curve.

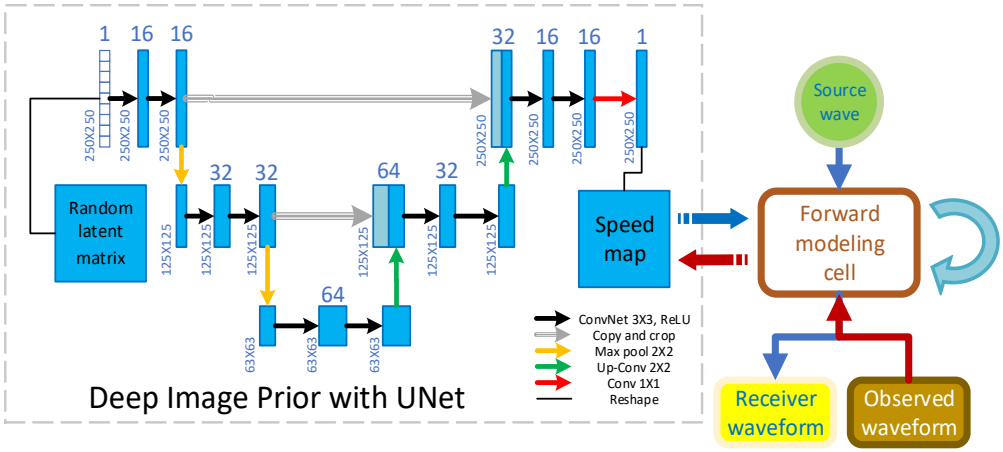

Figure 3.4 Structure of the unrolled RNN-FWI with DIP-UNet.

Table 3.2 RNN-FWI with DIP-UNet Architecture:

NN Layer	Architecture
Input	Random latent matrix (250×250)
Down Layer 1	{3×3 Convolutional layer (16) + LeakyReLU (0.1)} ×2 + Max pool (2×2) + BatchNorms
Down Layer 2	{3×3 Convolutional layer (32) + LeakyReLU (0.1)} ×2 + Max pool (2×2) + BatchNorms
Middle Layer 3	{3×3 Convolutional layer (64) + LeakyReLU (0.1)} ×2+ + BatchNorms
Up Layer 4	Up-Conv (2×2) + Copy and crop (Down Layer 2) + {3×3 Convolutional layer (32) + LeakyReLU (0.1)} ×2 + BatchNorms
Up Layer 5	Up-Conv (2×2) +Copy and crop (Down Layer 1) + {3×3 Convolutional layer (16) + LeakyReLU (0.1)} ×2 + BatchNorms
Output	3×3 Convolutional layer (1) + Sigmoid

3.3 Numerical simulation experiment

3.3.1 Comparison of automatic differentiation and adjoint state method

In this section, the primary task is to prove whether convolutional neural networks and automatic differentiation tools can be successfully integrated into the FWI architecture.

A one-dimensional velocity model is extracted from the cross section of Figure 2.8 dotted line place to compute the objective function gradient of the FWI or RNN-FWI. The setup of the experiment is the same as the first experiment in Chapter 2. Note that the experiment in this section is only to verify the equivalence of the two algorithms, so both algorithms use epochs of sufficient size to achieve complete convergence.

In Figure 3.5, the gradients at first iteration at each point in the 1D model computed using both automatic differentiation and adjoint state methods are compared, with the finite difference method being the true reference. As expected, the results were similar. The adjoint state method slightly overestimates the gradient, and the automatic differentiation method is consistent with the true gradient.

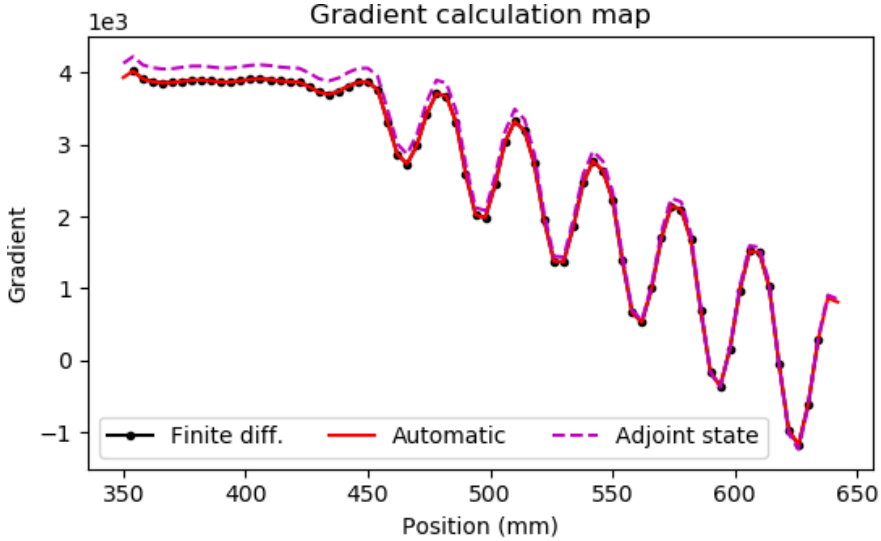

Figure 3.5 The first gradient map of the cost function with three approaches.

Next, we attempt to reconstruct the one-dimensional model using RNN-FWI of automatic differential method and FWI of adjoint state method.

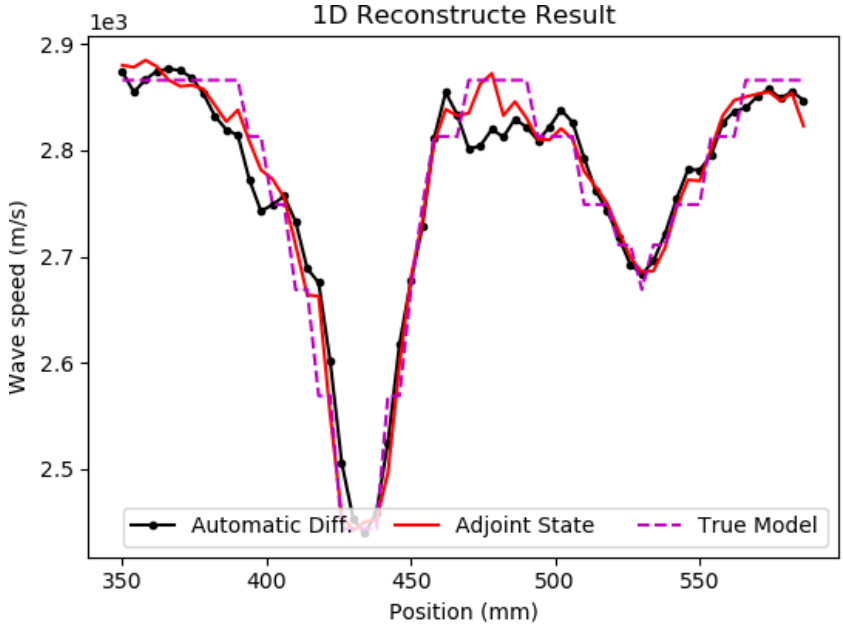

Figure 3.6 The inversion results with two approaches.

It can be seen that the two algorithms have obtained similar results, both in terms of boundary fitting and slope, which are quite consistent with the actual results.

Although gradient calculation shows that the adjoint state method overestimates the gradient, the optimization algorithm can effectively compensate for this defect, but it often requires additional calculation cycles to achieve it.

3.3.2 Imaging results based on different algorithms

In this section, we use the numerical simulation model in Chapter 2 and keep the same experimental settings. The conventional FWI of Adjoint state method + L-BFGS-B and RNN-FWI with ADAM, RNN-FWI with L-BFGS-B and Stochastic Gradient Descent are used to invert the model of Figure 2.5. The experimental Settings remained consistent, that is, 60 sensors were responsible for receiving and transmitting, and the EPOCH is 5. The profile of the reconstruction model is located in the dot lines of original model in Figure 3.7. It is worth noting that the purpose of this experiment is to compare the inversion accuracy of different algorithms, and no noise is added to the experimental data, so regularization factors are not added.

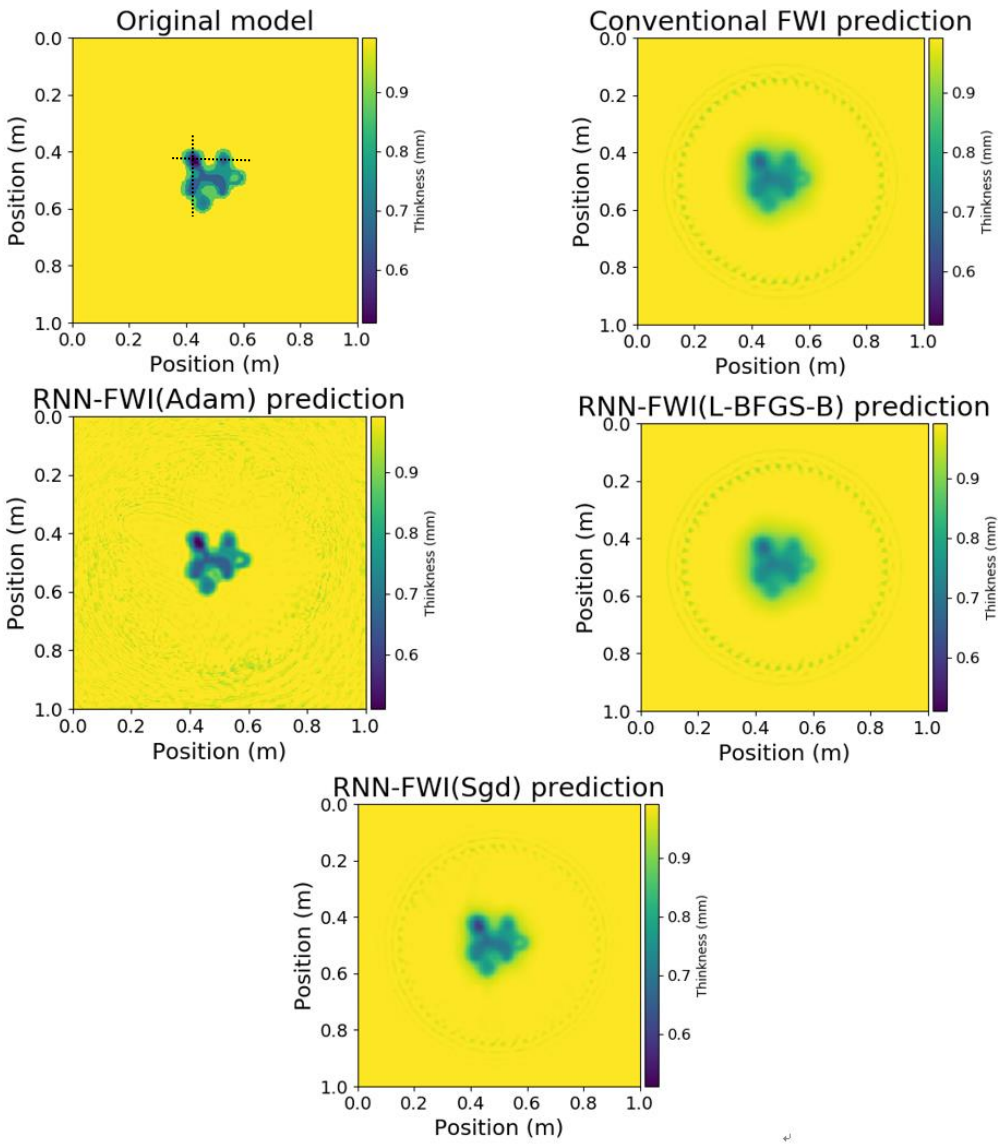

Figure 3.7 The inversion results with four algorithms.

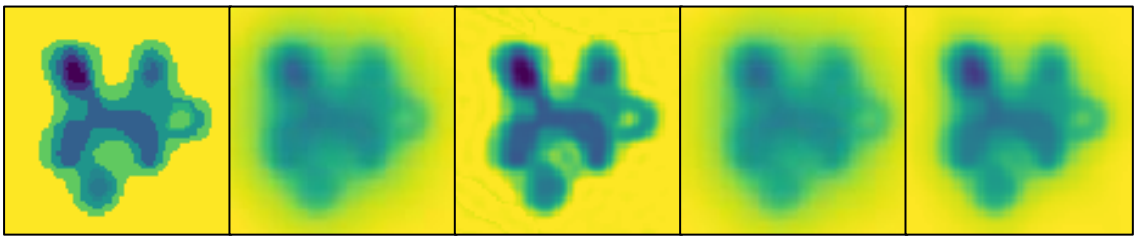

(a) (b) (c) (d) (e)

Figure 3.8 Enlarged view of central defect. (a)True model (b)Convention FWI (c)Adam (d)L-BFGS-B with RNN-FWI (e)SGD

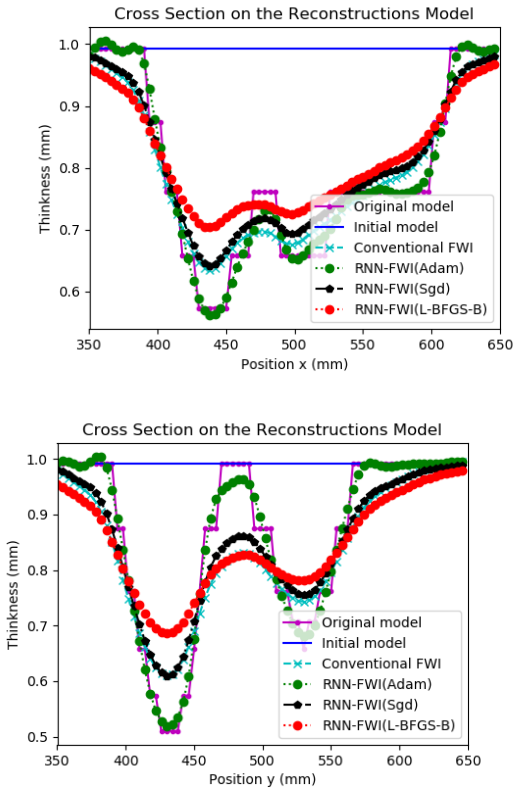

Figure 3.9 Results cross-sectional comparison diagram

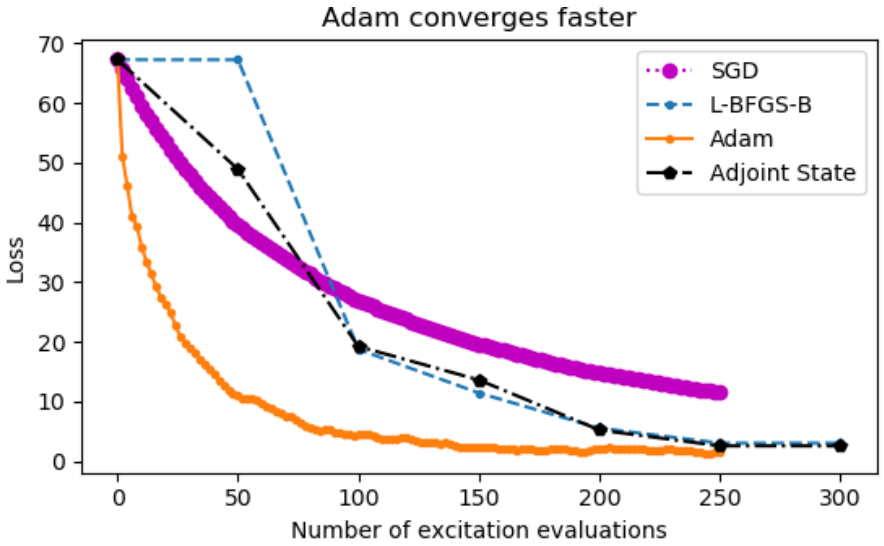

Figure 3.10 The loss functions with four approaches.

As can be seen from several figures, Adam has the fastest convergence, also has perfect results for corrosion edge and slope, and the calculation speed is better than other algorithms. It can be concluded from the convergence diagram that Adam+RNN-FWI has the fastest convergence speed, which is in line with the previous hypothesis. The optimization algorithm with the characteristics of self-adaptive momentum gradient step update and small batch data set can greatly accelerate convergence, and it

only needs about 2 epochs to achieve convergence, which is quite amazing. SGD has the slowest convergence, which can also be seen in Figure 3.8. SGD is also the most ambiguous reconstruction map. RNN-FWI or FWI with L-BFGS-B has similar convergence effects, and the results in Figure 3.8 and 3.9 are also consistent, proving that although RNN-FWI is a brand-new architecture, performance improvement still depends on some deep learning techniques. Although the final loss value Adam was close to L-BFGS-B on the convergence diagram, it can be seen from Figure 3.9 that the FWI depth reconstruction of L-BFGS-B algorithm was insufficient. In Figure 3.11, it converges to a certain threshold, the final reconstruction appears to be the same in all four algorithms, but the RNN-FWI (Adam) still shows a little bit better than others, but the convergence time of our proposed algorithm is better than other methods

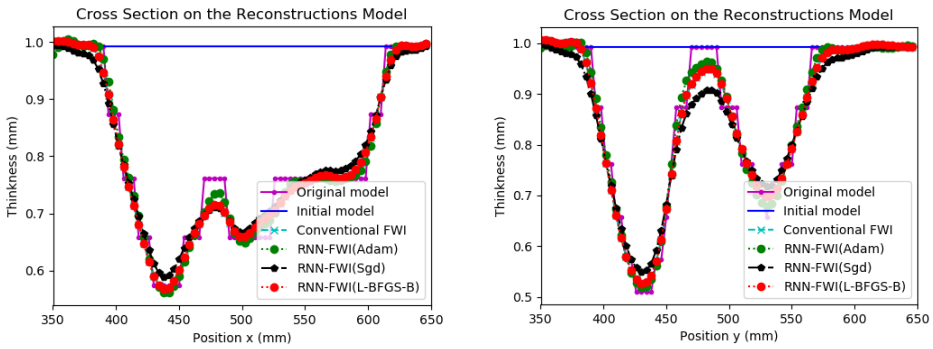

Figure 3.11 Results cross section comparison diagram (final convergence)

With the addition of GPU, the calculation speed has also been improved. It can be seen that the algorithm of L-BFGS-B has the slowest convergence, which is not difficult to explain, because this algorithm requires all data sets to participate in each calculation. Table 3.3 shows the calculation time of the four algorithms.

Table 3.3 Computation time table for different algorithm

Algorithm	Computation time
Conventional FWI	7min27s
RNN-FWI (Adam)	3min03s
RNN-FWI (SGD)	5min07s
RNN-FWI (L-BFGS-B)	6min51s

3.3.3 The effect of noise

This section investigates the robustness of the algorithm to noise. In order to facilitate the control of variables, we use the simulated value without adding noise for the original observation value here, and add gaussian noise to the synthetic data, according to the empirical value, the SNR of noisy waveform is -5 dB 0dB, 5dB. Usually the noise intensity is not greater than 0dB, but to test the robustness, -5dB noise is considered. In this experiment, we use two different algorithms to conduct comparative experiments, RNN-FWI (Adam+UNet) and conventional FWI (L-BFGS-B+TV). Fig. 17 is the waveform map which is added the noise. The corrosion model is consistent with previous experiment, the experimental setup is still responsible for receiving all sensors, in turn, launch the rest of the sensor, the initial velocity model is without damage uniform thickness of aluminum plate model. In this experiment, in order to compare the stability of different regularization algorithms for noise. we use two algorithms to conduct comparative experiments, Adam+ RNN-FWI +UNET regularization and L-BFGS-B +FWI+TV regularization tools.

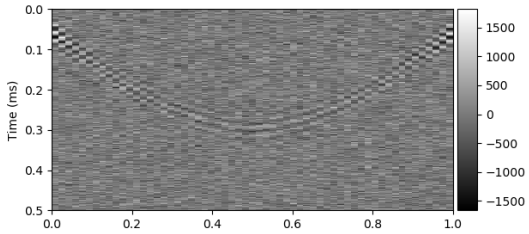

Figure 3.11 Received waves map (-5db SNR).

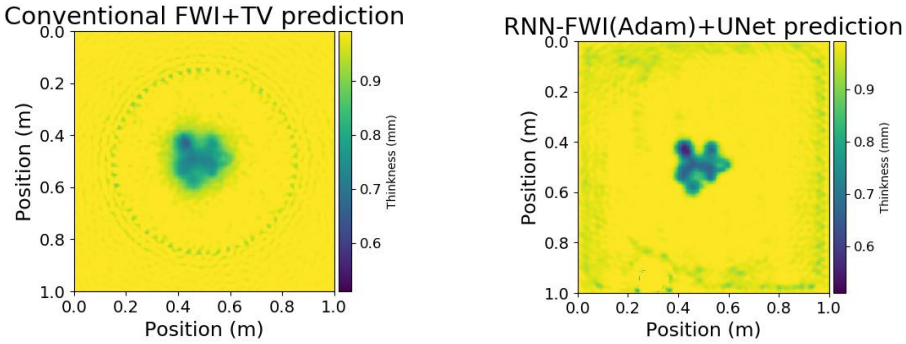

(a) (b)

Figure 3.12 Different methods results comparison (5dB) (a) RNN-FWI (Adam+UNet) (b) conventional FWI (L-BFGS-B+TV)

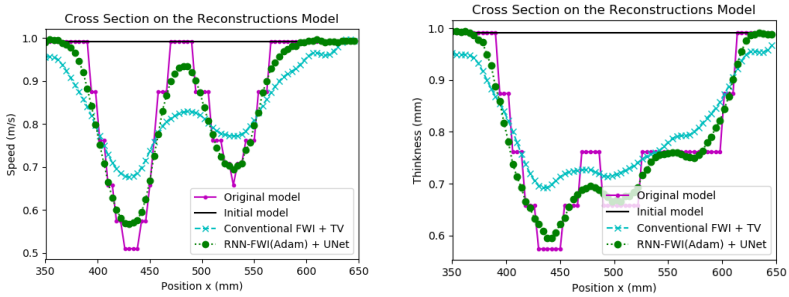

Figure 3.13 Results cross section comparison diagram (5dB)

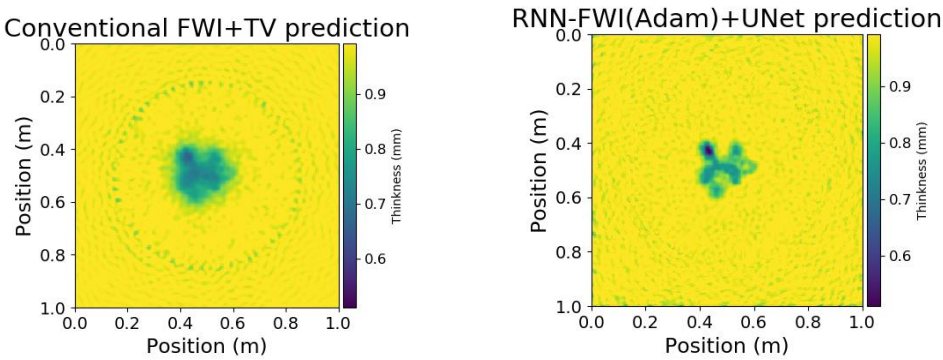

(a) (b)

Figure 3.14 Different methods results comparison (0dB) (a) RNN-FWI (Adam+UNet) (b) conventional FWI (L-BFGS-B+TV)

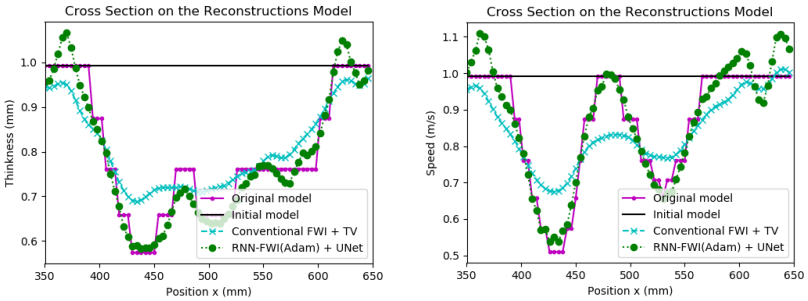

Figure 3.15 Results cross section comparison diagram (0dB)

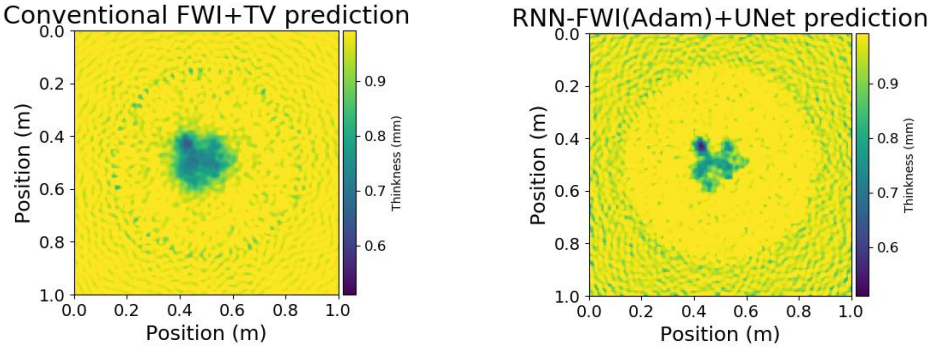

(a) (b)

Figure 3.16 Different methods results comparison (-5dB) (a) RNN-FWI (Adam+UNet) (b) conventional FWI (L-BFGS-B+TV)

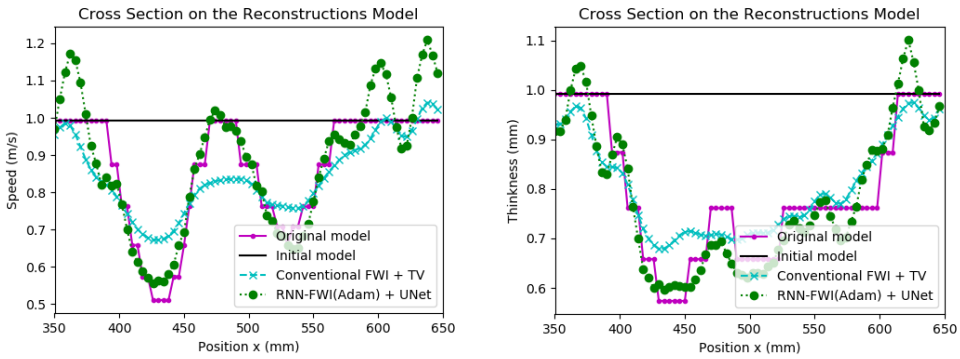

Figure 3.17 Results cross section comparison diagram (-5dB)

The reconstruction results of these four algorithms are shown in the figure above. The deep image prior regularization tools based on different CNN structures has played a good role. It can be seen from the figure that the inversion results of UNet are slightly better than that of conventional FWI. The artifacts caused by noise in the Figure 3.13 are more average, the corrosion profile is close to the real, and the UNet inversion result on the right side of the defect estimates the depth too lightly, but the two are generally better than the conventional FWI of the TV regularization tool, as shown in the Figure 3.14. It is intuitively found that the conventional algorithm does not reconstruct the real corrosion contour within the specified number of calculations, which may be caused by the 'reserved margin' feature of TV regularization. Under natural circumstances, the corrosion contour gradient should not change very drastically, so the conventional method is not as good as the above methods in the scope of application. As can be seen from Figure 3.15, Conventional FWI only inverts the approximate contour correctly, which is the worst among all imaging results. In contrast, RNN-FWI results showed much less deterioration. We further analyzed the inversion quality through three indicators in Table 3.4: PSNR (peak signal-to-noise ratio) and SSIM (structural similarity indicator measure).

Table 3.4 Inversion quality at different evaluation index (with -5dB noise)

Algorithm	SSIM	PSNR
RNN-FWI (Adam+UNet)	0.981	48.6
Conventional FWI (L-BFGS-B+TV)	0.920	44.3

Compared with conventional FWI, the improved inversion results of RNN-FWI

for noise data are verified. This comparison proves the regularization effect of generative neural network with depth image prior. In the presence of noise, the inversion results of RNN-FWI are smoother and more robust than those of conventional FWI.

3.4 Conclusion

In this chapter, by observing the algorithm structure of conventional FWI in last chapter, discovering the similar characteristics of RNN and FWI, we introduce RNN into FWI, and form a new algorithm. RNN-FWI brings many new technologies and techniques of deep learning into conventional FWI, including automatic differentiation instead of adjoint state method, and depth image prior instead of TV regularization, and the Adam algorithm instead of the quasi-Newton method, which bring the possibility of comprehensively improving the algorithm. This chapter provides a theoretical basis for later experiments. The first experiment verified the consistency of automatic differentiation and the adjoint state method for calculating gradients. Then the performance of different algorithms for the same defect and the robustness of different regularized tools for noise are compared.

Chapter 4 Actual Experiment

4.1 Introduction

In the algorithm research of the previous chapters, we concluded that Adam+RNN-FWI+Unet algorithm has better performance than any other algorithm. In this section, we will introduce the preparation and details of the actual experiment in turn, and then process the data obtained from the actual experiment, and input the experimental data into different algorithms for comparison.

4.2 Actual experiments setup

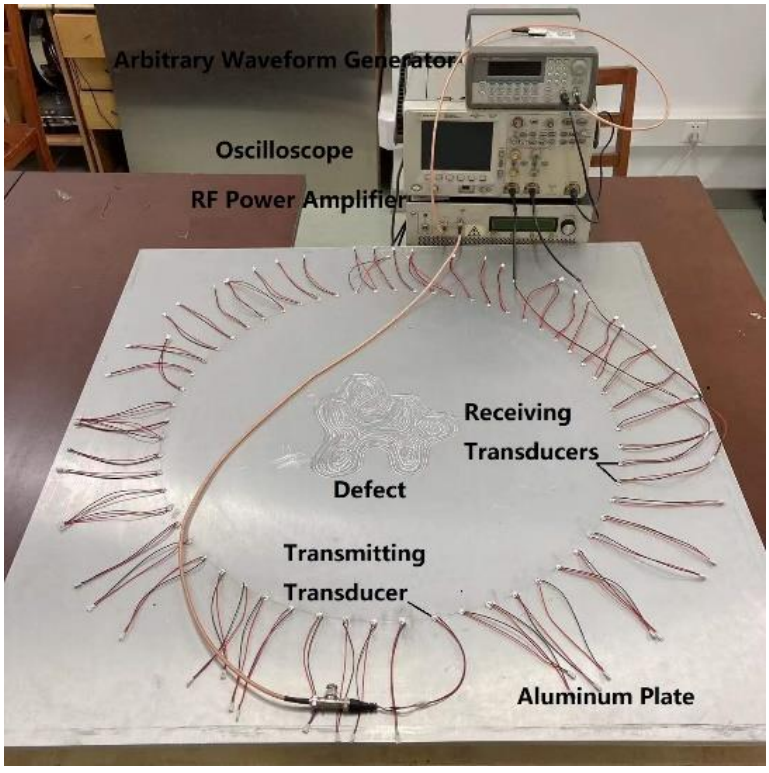

Figure 4.1 Actual experimental equipment setup.

The experimental device is shown in Figure 4.1. It is carried out on a 1000*1000*10mm 6061(Aluminum material label) aluminum plate, the plate is supported by a rotating platform for easy operation and measurement. The corrosion on the plate consist of a series of 1mm, 0.5mm ,0.25mm depth irregular defects, the deepest defect is half of the plate thickness, the defect wall and the plate surface form a 30°

angle to avoid the A0 mode to S0 mode conversion, the corrosion was designed by CAD software and sculptured by CNC, ensuring a high degree of agreement with the numerically simulated model. There is a circle like transductor array with a diameter of 700mm on the metal plate surface around corrosion, and 60 PZT-5 transductors with a central frequency of about 50khz are evenly glued to the aluminum plate with epoxy resin to form the circle array, all the PZT transductors can transmit and receive supersonic wave. The Lamb wave transmission signal is generated by an Agilent 33220A arbitrary waveform generator, amplified by the RF power amplifier of AG Series Amplifier 1011(T&C Power Conversion, Inc.), and the PZT signal is collected by an Agilent MSO6052A mixed signal oscilloscope. The calculation of FWI was done by a computer with CPU as i7 9700k, memory as 16G DDR4, and GPU as Nvidia GTX1080ti 11GB.

Each PZT transductor collects 0.5ms waveform information, which is divided into 1000 points for storage. After the data collection is completed, the comparison between the actual raw acquisition waveform and the numerical simulation is shown in Figure 4.2, it can be seen that in the direct wave area, the phase difference between the two is basically barely existed. It is necessary to limit the bandwidth of the collected signal to remove clutter with frequencies other than 45 to 65 Khz, we use a third order Butterworth bandpass filter to filter the signal. Then the first arriving A0 wave packet and defect scattered wave are gated to block boundary echo and other clutter interference, we use a flat-topped Hamming window to achieve gating, which can effectively prevent spectrum leakage. We only need to add different delays to such window and multiply the processed signal for signal processing. Figure 4.3 is the comparison between the signal processed and the simulated signal. It can be seen that the actual experiment and the simulated experiment highly overlap, which can verify the success of the forward algorithm from one side. The velocity map of the aluminum plate is the same as the model used in the numerical simulation in Chapter 2

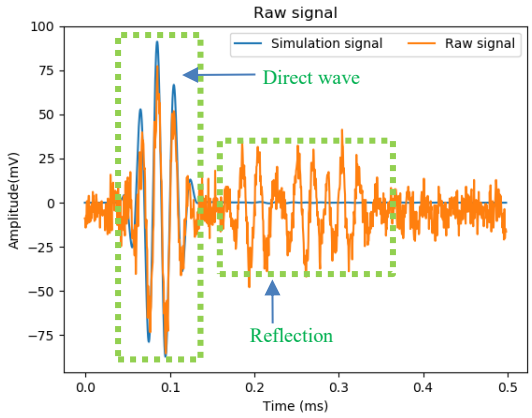

Figure 4.2 Actual experimental waveform and simulation waveform.

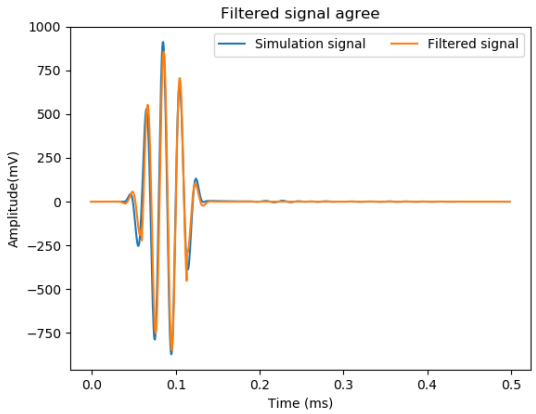

Figure 4.3 Filtered and windowed waveform and simulation waveform.

4.3 Actual experiment data in different algorithms

In the experimental configuration of the previous chapter, the experiment is carried out. After the data is collected, the filtering process is performed, and the RNN-FWI is used to reconstruct the velocity model. The initial model is a non-damaged aluminum plate model with uniform thickness. The comparison diagram in Figure 4.4 and 4.5 below is the result of RNN-FWI using Adam and UNet, and the conventional FWI with TV and L-BFGS-B respectively.

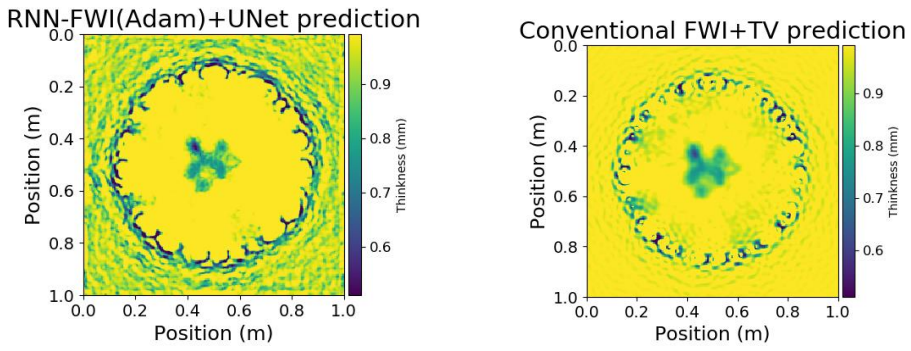

(a) (b)

Figure 4.4 Actual experiment imaging result. (a) RNN-FWI with Adam+UNet (b) Conventional FWI with TV

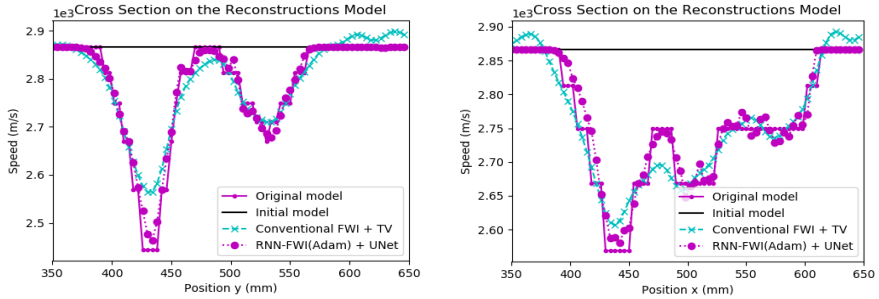

Figure 4.5 Cross section comparison results

The algorithm we present in this paper is inputted actual experiment data as observed data, although the filter window filtered out the echo signal, our RNN - FWI is still relatively real portray the shape of the corrosion. At some thin defect position, inversion depth is not so reliable to the real depth value, but compared with the traditional algorithm, the improvement in accuracy and robustness is significant.

4.4 The effect of different number of transductors

The number of transductors in a ring array to extract enough signals from a wavefield can be expressed as：

$$N > \frac{4\pi r}{\lambda} \tag{4.1}$$

where r is the radius. At out experiment setup, almost 135 transducers would be needed to correctly reconstruct the image. However, it is obviously not realistic that the experiment requires so many transductors, so the experimental setup is completed by 60 transductors. The installation of so many transductors limits the performance of real-

time non-destructive testing in industrial pipelines production, so in this subsection we study on impact of imaging with different numbers of transductors. We can derive the number from the trade-off between the number of PZT and the number of transductors. In Figure 4.6 4.7 4.8 4.9 are the inversion results of 60, 30, 20 and 15 PZTs, respectively. In this experiment, Adam+RNN-FWI was used for imaging.

It is worth noting that in this section we use simulated data as our data in order to avoid some unexpected situations

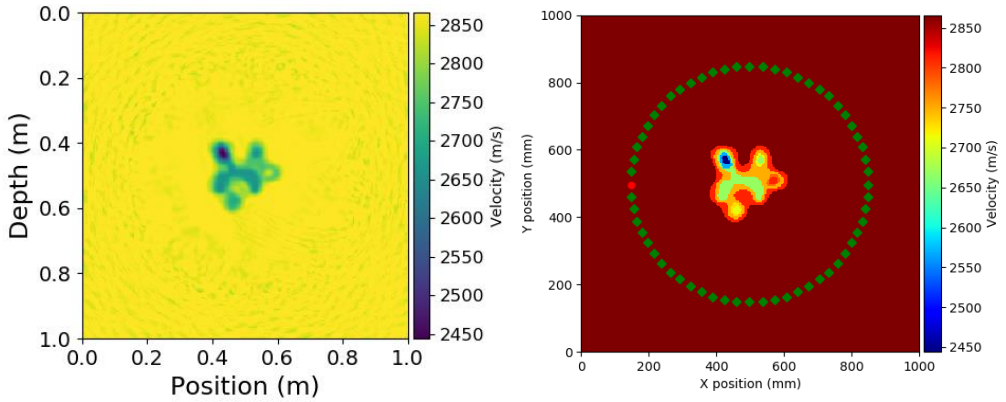

Figure 4.6 60 transducers

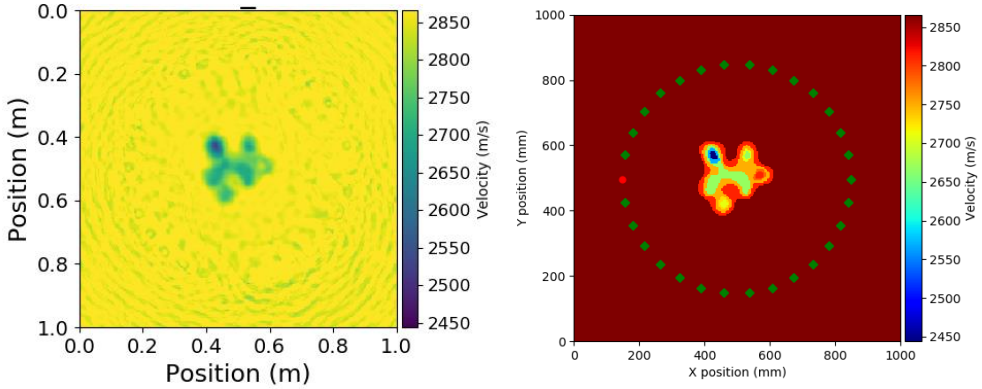

Figure 4.7 30 transducers

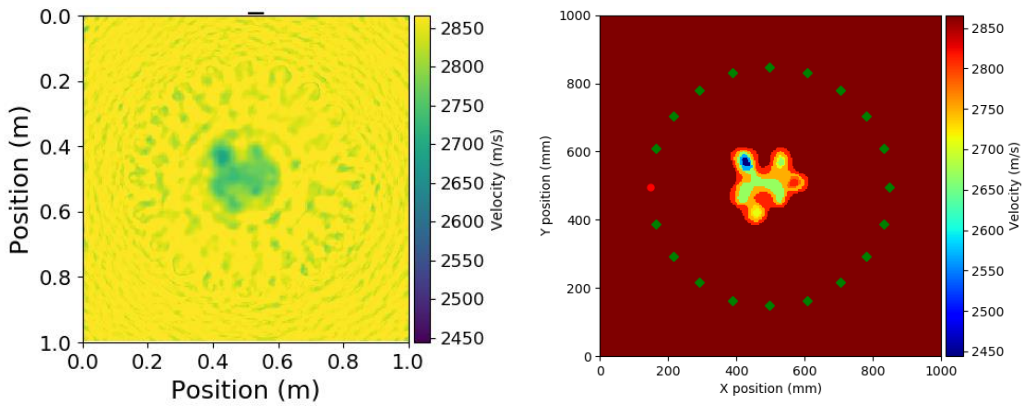

Figure 4.8 20 transducers

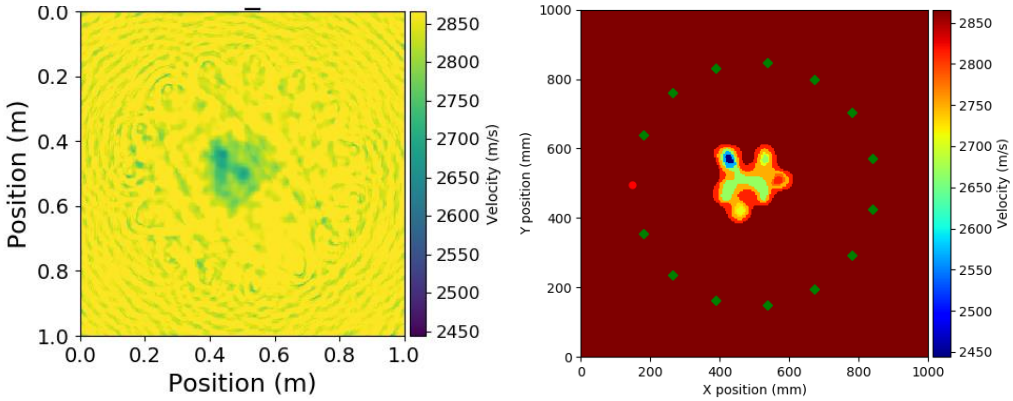

Figure 4.9 15 transducers

It can be observed that both 60 and 30 sensors involved in the experiment can carry out accurate imaging of corrosion, while less than 30 sensors not only inversion produces artifacts, but also failed to reconstruct the real corrosion.

We also investigate the ability of semicircular receiver arrays to reconstruct corrosion models. Experimental background is in the actual experiments, many researchers have found that the actual experiment of direct extraction of signal energy is greater than that of defect echo energy, a lot of useful reflection submerged by noise and boundary of the echo signal, eventually forced removed by the signal process procedure, so, the experiment is set up to have 19, 29 and 45 receiving sensors in a semicircle opposite to the transmitting sensor.

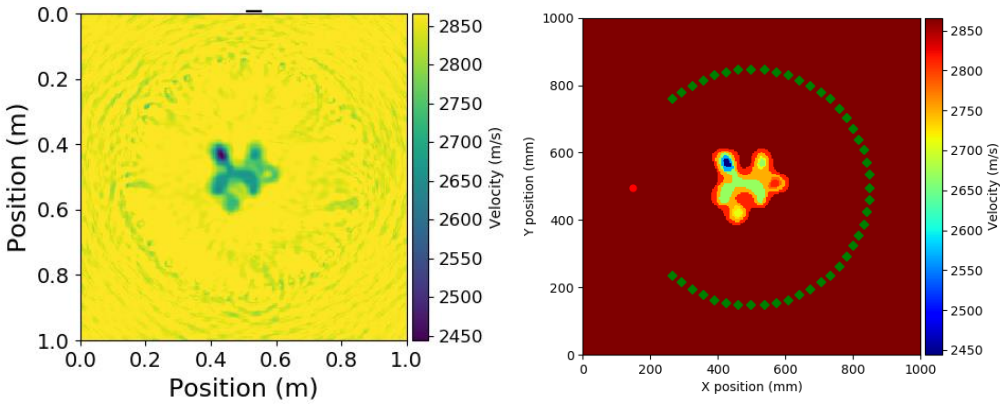

Figure 4.10 45 transducers in half circle transducer array

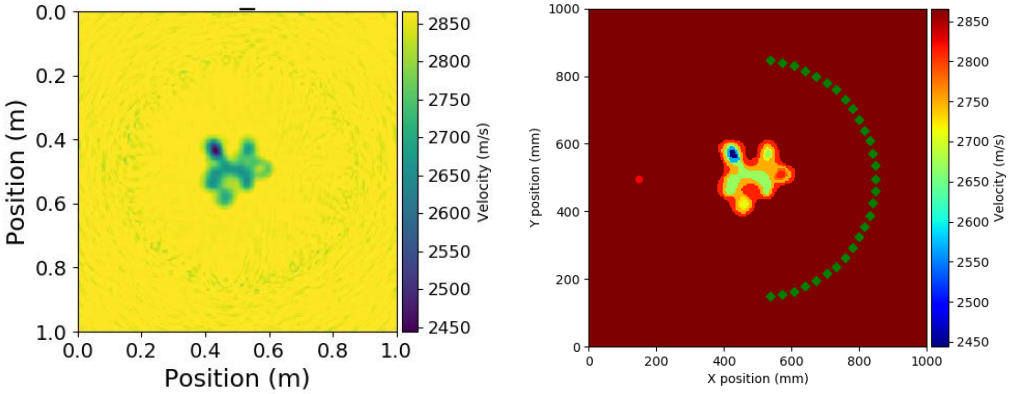

Figure 4.11 29 transducers in half circle transducer array

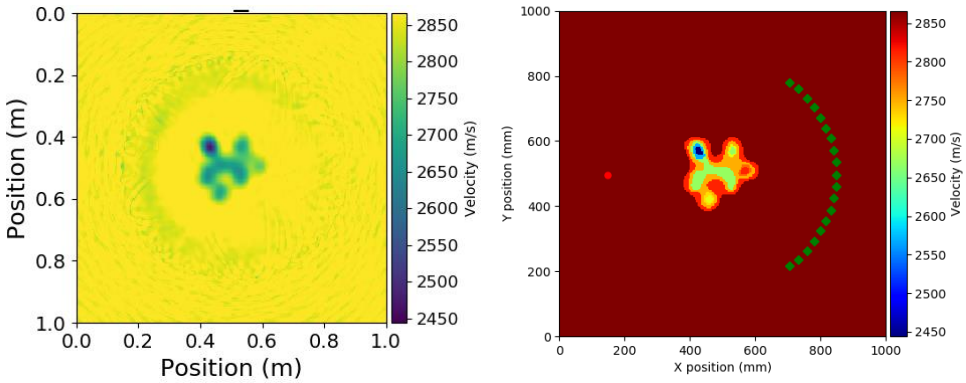

Figure 4.12 19 transducers in half circle transducer array

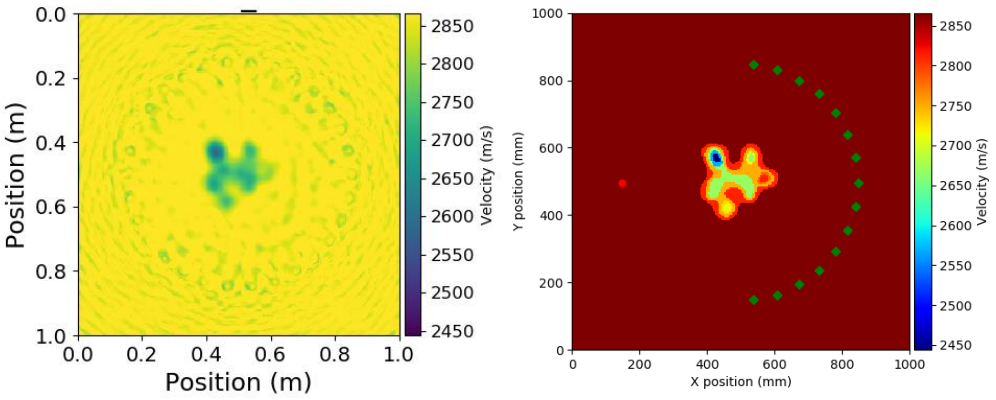

Figure 4.13 15 transducers in half circle transducer array

The experimental results can show that the semi-circular sensor array does not have much degrade effect on the accurate inversion model. We reduce from 45 sensors to 15 sensors, and the experimental results do not change drastically, relying on the computational accuracy of 45 receiving sensors is almost the same as that of 60 sensors, the experimental accuracy of 15 sensors does not drop much.

Experiments have shown that we can reduce the number of acquired waveforms and reduce the computational complexity without losing too much precision. This has practical significance for the improvement of experimental calculation speed. Observe the difference between the experimental observation value and the simulated value under the setting of Figure 4.6 (right), as shown in 4.14, the gradient update is calculated from this figure, and the obvious waveform in the figure appears in the center, that is to say, the gradient update It mainly relies on straight-line propagation, and the length of the yellow frame accounts for one-fifth of the total length, which means that only one-fifth of the sensors can be used to achieve the results obtained by the data collected by all the sensors without losing too much accuracy.

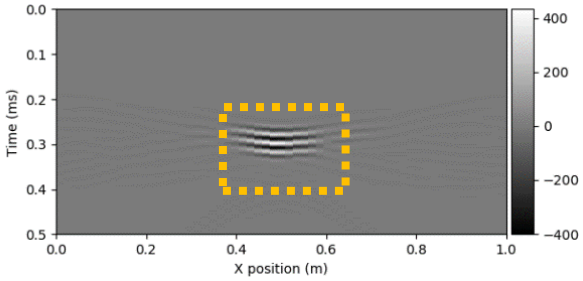

Figure 4.14 The difference between simulated and observed values

4.5 Studies of different initial models

When the difference between the initial velocity model and the real velocity model is too large, the conventional FWI with an objective function of L2 distance occurs the problem of cycle jumping. When the phase difference between the predicted data and the real data is greater than half a cycle, resulting in failure to converge. As the objective function, W2 can effectively overcome the above situation.

Two values far away from the true thickness are selected as the thickness of the initial model, and the velocity without defects is 2866m/s, the velocity model with uniform velocity of 2600m/s and 3000m/s is set as the initial model for iteration, where the phase difference is much greater than half cycle. Here we choose the simulated value as the observed value for iterative calculation.

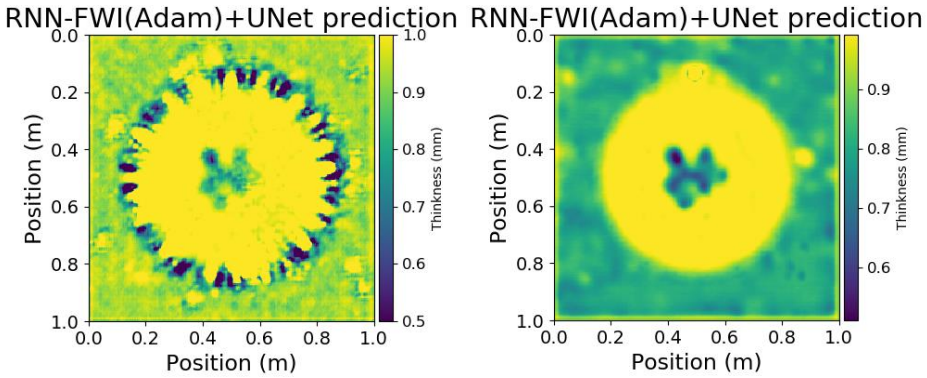

(a) (b)

Figure 4.17 Imaging result maps (2600m/s initial model) (a) actual experiment(b) simulation experiment (2600m/s)

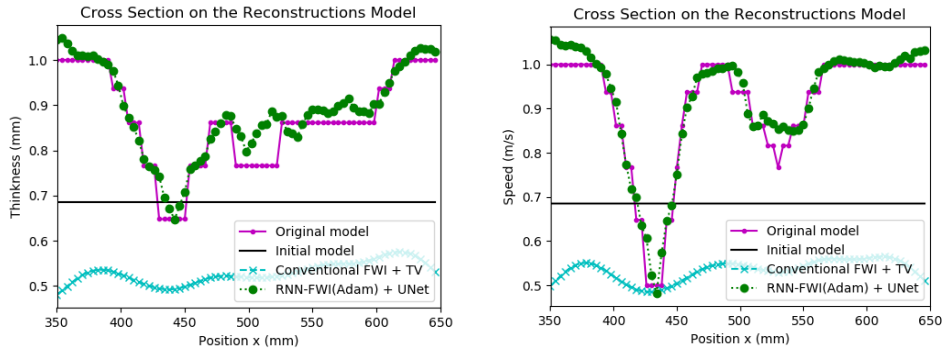

Figure 4.18 Results cross section comparison diagram in actual experiment

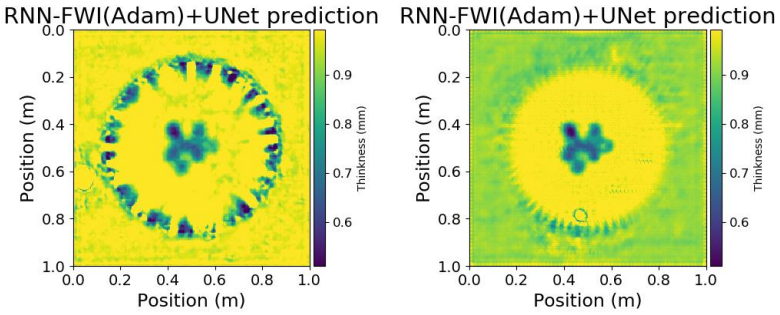

Figure 4.19 The loss functions with two approaches in noises

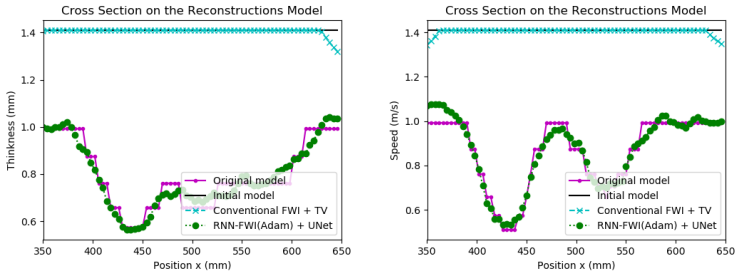

Figure 4.20 The loss functions with two approaches in noises

By observing all the above results, it can be shown that FWI with W2 distance as objective function can normally converge to relatively accurate results within a certain initial velocity range. However, neither of the conventional methods (blue line) can be used to reconstruct the model in these two initial velocity models.

4.6 Conclusion

In this chapter, we introduce the details of the preparation process of the actual experiment. The preparation of materials, the setting of the sensor, the model of the experimental instrument, the preparation process of the experiment, and finally the signal preprocessing of the actual experiment is also introduced at the same time. Finally, we conducted a series of experiments using the data collected in the experiment, and the experimental results of the experimental data proved the practical significance of our proposed algorithm. Finally, we also studied some problems with actual experimental background, including the influence of the number of sensors and position on the inversion image.

Chapter 5 Conclusion and Prospect

This paper proposes a new guided wave tomography technology based on the framework of deep learning, analyzed the similarities, advantages and disadvantages of deep learning neural network and FWI, and successfully combines neural network with full waveform inversion, using the powerful nonlinear inverse ability of neural network algorithm to optimize conventional FWI. The structure of RNN-FWI is roughly the same as that of conventional FWI, the difference is that the forward modeling unit of single step is represented by the RNN operation unit, in the meanwhile, realized the idea of automatic differentiation instead of adjoint state method to calculate gradient, and a CNN-based network acted as the regularization of the objective function. The W2 distance utilizes the waveform phase difference and the amplitude difference as the updated parameters, which alleviates the effects of artifacts and non-convergence caused by the cycle jump to a certain extent.

In the actual experiment, the performance of RNN-FWI with several optimization algorithms such as Adam and conventional FWI was compared and analyzed, and the conclusion was drawn from the numerical simulation and actual experiment that RNN-FWI greatly avoided the probability of inversion falling into local minima and enhanced robustness because of deep neural network and regularization tools, and also got rid of the highly dependence on the initial speed model, the automatic differentiation reduced the system error caused by conventional algorithms, the BP algorithm reduces the complexity of explicitly solving the gradient, the Adam optimization algorithm accelerated the convergence speed and reduced the memory usage, the convolution kernel reduce the forward modeling computational complexity. More details of the improvement in combining deep learning with full waveform inversion will be investigated in future work.

Full waveform inversion based on recurrent neural network introduces many optimizations and advantages of deep learning into conventional full waveform inversion, and it is proved by practical experiments that RNN-FWI has many

advantages over conventional FWI, including: the inversion accuracy is improved, decreases the demand of the accurate initial model provided by algorithms such as traveltime tomography, and the imaging is not easily affected by local minima, besides that, the deep learning framework (TensorFlow) will make it more convenient to perform calculations on GPUs and even distributed computer clusters.

The advantage of using small batch data global optimization of ADAM is that it does not require conventional frequency domain FWI low-frequency to high-frequency iterative calculation to prevent falling into local minimum and cycle skipping effect. ADAM is first-order optimization method which means it does not calculate the Hessian matrix, does not require all data to participate in once calculation, this greatly reduced memory consumption and speed up the calculation. At the same time, the automatic differentiation used in deep learning solving gradient is equivalent to the adjoint state method which demonstrated in formula before. Due to the absence of systematic errors caused by adjoint state method, the inversion accuracy is also improved, the convolution kernel optimized by the deep learning framework (TensorFlow) replaces the manual spatial derivation to reduce the forward modeling computational complexity.

Regularization tools (deep image prior) can naturally introduce spatial correlation as regularization into the generated velocity model, thereby suppressing noise in gradients calculating and mitigating local minima phenomenon, and significantly improving inversion in the presence of noise, strengthening the robustness to noise polluted signal. And there is no need for additional training data and iteration computation in regularization, thus enhance the utility of the entire algorithm and without adding computational complexity to the entire algorithm. Compared with conventional regularization algorithms, such as TV, the regularization tool based on deep image prior does not need smoothing parameters and weight parameters set based on human experience values, which makes the whole algorithm more automatic and avoids some human errors. Therefore, the overall regularization effect is better than the conventional algorithm. In addition, regular tools based on deep image prior provide a development direction based on deep learning. Subsequent studies can add dropout

layers to existing networks, making RNN-FWI a more effective method to estimate uncertainties in the high-dimensional model space of velocity estimation.

Compared with algorithms that need to be trained in advance, such as algorithms that use CNN or SDM to learn the hidden mathematical parameters or direction of gradient descent, RNN-FWI does not need to prepare large batch of dataset, because the forward operator contains physical prior information (acoustic wave formula), training is not required, and the accuracy is very high naturally. Similarly, as for the datasets of the pre-training algorithm, it is difficult to generate or collect datasets with all types of shapes and depths of defects or corrosions, which is the primary difficulty of the pre-training algorithm. Moreover, the parameter models generated by existing pre-training algorithms are very large (because of the huge number of datasets), which is still a challenge for offline hardware applications.

Using automatic differentiation and BP algorithm to compute the gradient of the cost function has several advantages. Foremost among them is that it greatly reduces development time, as it avoids the need to manually implement and validate adjoint state methods, and more easily incorporate some deep learning optimization and computational tricks. However, the main disadvantage is that it is memory-intensive, as it stores all wavefield time slices in memory. In FWI, the wavefield at the final time step will definitely be affected by the wavefield and the model at the initial time step, so backpropagation must occur throughout the whole sequence of time steps, which is very memory-intensive, so instead of storing them, we resort to regenerating the wavefields during backpropagation, which is a memory vs. computation time trade-off.

Although RNN-FWI has many of the above advantages, it only slightly improves the resolution, that is, only improves the accuracy and resolution in terms of reducing system errors. It does not improve the accuracy theoretically from physics mechanism. Therefore there is still improve subsequent research can be developed that excitation supersonic wave can be replaced with higher frequency one, the currently available option is the SH mode PZT transductors with different polarization directions and shorter wavelength to improve the resolution of FWI, and at the same time, the introduction of the SH0 mode which without dispersion is more conducive to the

detection of cracks or crack-like damage, the joint algorithm of the two should have wider versatility and practicality. Another research direction that can improve the resolution is to combine beamforming and full waveform inversion. Beamforming takes advantage of the high precision brought by the reverse-time scanning of the transductor array and can be combined with FWI to further improve resolution. On the other hand, ring shape like transductors array may be limited by size in practical applications, so it is also very meaningful to develop a single-side transceiver or contra-side transceiver transductor array for beamforming full waveform inversion.

Reference

[1] Li J W, Chen J M. Nondestructive Testing Manual. Beijing: China Machine Press, 2002.1.

[2] Groysman A. Corrosion for Everybody. Springer, New York, 2010.

[3] Demer L. Appeals court gives go-ahead to BP investor suit over 2006 alaska oil spills. http://www.adn.com/article/20140213/appeals-court-gives-go-ahead-bpinvestor-suit-over-2006-alaska-oil-spills, 2014.

[4] Yang L, Ume I C. Inspection of notch depths in thin structures using transmission coefficients of laser-generated Lamb waves. Ultrasonics, 2015, 63: 168-173.

[5] Ng C T. A two-stage approach for quantitative damage imaging in metallic plates using Lamb waves [J]. Earthq Struct, 2015, 8(4): 821-841.

[6] Ho K S, Billson D R, D.A. Hutchins. Ultrasonic Lamb wave tomography using scanned EMATs and wavelet processing [J]. Nondestruct Test Eva, 2007, 22(1): 19-34.

[7] Liu Z Q. Ultrasonic Lamb waves in nondestructive testing. Nondestructive testing. 1999, 21(9): 409-423.

[8] Jiang F T, He S Q and Shen J Z. Discussion on some problems in Lamb wave flaw detection [J]. Materials Engineering, 1996, 41(10):29-31.

[9] Takeji E, Tadanobu T. GB2108-80 Lamb wave flaw detection method for thin steel plates.

[10] GB8651-88 Ultrasonic wave flaw detection method for metal sheet, Chinese National Stardard.

[11] QJ1269-87 Lamb wave flaw detection method for sheet metal, Chinese Industrial Standard.

[12] Lamb H. On the Waves in an Elastic Plate. Proceedings of the Royal Society of London, 1917:293-312.

[13] Akenbach. Propagation of waves in elastic solids. Shanghai: Tongji University Press, 1992. Translated by Z.X Xu and J.R Hong.

[14] Ying C F, Zhang S Y and Shen J Z. Ultrasonic scattering in solids. Beijing: National Defense Industry Press, 1994.

[15] Chimenti D E and Martin R W. Nondestructive evaluation of composite laminates by leaky lamb waves. Ultrasonics. 1991， 29(5):13-21.

[16] Worlton D C. Experimental Confirmation of Lamb Waves at Megacycle Frequencies, Journal of Applied Physics, 1961, 32(6):967-971.

[17] Rayleigh J. The theory of sound. Vol.I and II, New York: Dover Publication, 1945.
[18] Love A. A treatise on the mathematical theory of elasticity. New York: Dover Publications, 1944.
[19] Mirsky L, Herrmann G. Axially symmetric motions of thick cylindrical shells. Journal of Applied Mechanics, 1958(80):97~102.
[20] Sachse W, Pao Y H. On the determination of phase and group velocities of dispersive waves in solids，J.Appl.Phys，1978，49(8)，4320-4327.
[21] Veidt M, Saehse W. Ultrasonic point-source/point-receiver measurement in thin specimens, J. Aeoust. Soe. Am, 1994, 96(4)2318-2326
[22] Alleynem D, Cawley P. A two-dimensional Fourier transform method for the measurement of propagating multimode signals. J. Acoust. Soe. A. M, 1991, 89
[23] Grondel S, Delebarre C, Assaad J. Modeling of Lamb wave generation for application in health monitoring of composite plates. Ultrasonic Symposium, 2001
[24] Saravanos D A, Heyliger P R. Coupled Layerwise Analysis of Composite Beams with Embedded Piezoelectric Sensors and Actuators, Journal of Intelligent Material Systems and Structures, 1995, (6):350-362.
[25] Rohde A, Veidt M, Rose L, Homer J. A computer simulation study of imaging flexural inhomogeneities using plate-wave diffraction tomography. Ultrasonics. 2008, 48: 6–15
[26] Belanger P, Cawley P. Feasibility of low frequency straight-ray guided wave tomography. NDT&E International. 2009, 42: 113-119
[27] Yu M, Lan C Q. et al. Experimental study on Lamb wave CT imaging[J]. Acoustics Technology,1999,14(4):162-164
[28] Liu Z Q, Ta D. Recognition of Lamb wave modes by two-dimensional Fourier transform[J].Acoustics Technology,2000,19(4):212-219.
[29] Huang S L, Wei Z, Zhao W and Wang S. A New Omni-Directional EMAT for Ultrasonic Lamb Wave Tomogrephy Imaging of Metallic Plate Defects. Sensors 2014, 14,3458-3476; doi:10.3390/s140203458
[30] Volker A, Bloom J. Experimental results of guided wave travel time tomography. Rev. Prog. Quant. Nondestruct. Eval., 30:215–222, 2011
[31] Earle P S, Shearer P M. Characterization of global seismograms using an automatic-picking algorithm. Bull. Seismol. Soc. Am., 84:366–376, 1994.
[32] Li S, Jackowski M. Refraction corrected transmission ultrasound computed tomography for application in breast imaging. Med.Phys., 37:2233–2246, 2010.

[33] Huthwaite P. Evaluation of inversion approaches for guided wave thickness mapping. Proc. R. Soc. A., 470:20140063, 2014.

[34] Huthwaite P, Simonetti F. High-resolution guided wave tomography. Wave Motion, 50(5):979–993, 2013.

[35] Huthwaite P. Evaluation of inversion approaches for guided wave thickness mapping. Proc. R. Soc. A., 470:20140063, 2014.

[36] Rao J, Ratassepp M, Fan Z. "Guided Wave Tomography Based on Full-Waveform Inversion." IEEE transactions on Ultrasonics, Ferroelectrics, and Frequency Control, 63(5):737-745, 2016.

[37] Tarantola A. Linearized Inversion of Seismic Reflection Data[J]. Geophysical Prospecting, 1984, 32(6): 998-1015.

[38] Tarantola A. Inversion of seismic reflection data in the acoustic approximation[J]. Geophysics, 1984, 49(8): 1259-1266.

[39] Tarantola A. A strategy for nonlinear elastic inversion of seismic reflection data[J]. Geophysics, 1986, 51(10): 1893-1903.

[40] Gauthier O, Virieux J, Tarantola A. Two-dimensional nonlinear inversion of seismic waveforms: Numerical results[J]. Geophysics, 1986, 51(7): 1387-1403.

[41] Mora P. Nonlinear two-dimensional elastic inversion of multi-offset seismic data[J]. Geophysics. 1987, 52(9): 1211-1228.

[42] Bunks C, Saleck F M, Zaleski S. Multiscale seismic waveform inversion[J]. Geophysics, 1995, 60(5): 1457-1473.

[43] Pratt R G. Seismic waveform inversion in the frequency domain, Part I: theory and verification in a physical scale model[J]. Geophysics, 1999, 64(3): 888-901.

[44] Sirgue L, Pratt R. G. Efficient waveform inversion and imaging: A strategy for selecting temporal frequencies. Geophysics, 2004, 69(1): 231-248.

[45] Shin C, Ha W. A comparison between the behavior of objective functions for waveform inversion in the frequency and Laplace domains[J]. Geophysics, 2008, 73(5): VE119-VE133.

[46] Cho Y, Ha W, Kim Y. Laplace–Fourier-Domain Full Waveform Inversion of Deep-Sea Seismic Data Acquired with Limited Offsets[J]. Pure & Applied Geophysics, 2016, 173(3): 749-773.

[47] Bozdağ E, Trampert J, Tromp J. Misfit functions for full waveform inversion based on instantaneous phase and envelope measurements[J]. Geophysical Journal International, 2011, 185(2):845-870.

[48] Rao J, Ratassepp M, Fan Z. Investigation of The Reconstruction Accuracy of Guided Wave Tomography Using Full Waveform Inversion. Journal of Sound and Vibration, 400:317-328, 2017.

[49] Lin M, Liu Y. Guided Wave Tomography Based on Supervised Descent Method for Quantitative Corrosion Imaging. IEEE Trans Ultrason Ferroelectr Freq Control. 2021 Dec;68(12):3624-3636.

[50] Xu X N, Yu Z J, Zhu L Q. A graphical method to solve a dispersion equation of Lamb wave, JOURNAL OF ELECTRONIC MEASUREMENT AND INSTRUMENT, 2012 11, Vol. 26: 966-971

[51] Rose F and Wang C H. Mindlin plate theory for damage detection: Imaging of flexural inhomogeneities. J. Acoust. Soc. Am., 127(2):754–763, 2010.

[52] Berenger J P. A perfectly matched layer for absorption of electromagnetic waves. J. Comput. Phys., 114:185–200, 1994.

[53] Plessix R. E. A review of the adjoint-state method for computing the gradient of a functional with geophysical applications. Geophys. J. Int., 167:495–503, 2006.

[54] Yedlin M J, Van D. Vorst, 2010, Tutorial on the continuous and discrete adjoint state method and basic implementation: CREWES Research Report, 22, 1–20.

[55] Liu Q, Tromp J. 2006, Finite-frequency kernels based on adjoint methods: Bulletin of the Seismological Society of America, 96, 2383–2397.

[56] Pratt R G, Shin C, Hicks G J. Gauss-newton and full newton methods in frequency-space seismic waveform inversion. Geophys. J. Int., 133:341–362, 1998.

[57] Morales J L, Nocedal J. 2011, Remark on “algorithm 778: L-BFGS-B: Fortran subroutines for large-scale bound constrained optimization”: ACM Transactions on Mathematical Software (TOMS), 38, 7

[58] Esser E, Guasch L, Leeuwen T V. 2016b, Total-variation regularization strategies in full-waveform inversion: arXiv preprint arXiv:1608.06159.

[59] Sun J, Niu Z, Innanen K A. A theory-guided deep learning formulation of seismic waveform inversion[C]. SEG Technical Program Expanded Abstracts, 2019: 2343-2347.

[60] Liu J G, Xu K L. Automatic Differentiation and Its Application in Physical Simulation, Acta Phys. Sin. Vol. 70, No. 14 (2021)- 149402

[61] Perfectly matched layer theory and its application in wave simulation calculation, Journal of Yili Normal University(Natural Science Edition), Sept.2020 Vol.14 No.3

[62] Ulyanov D, Vedaldi A, Lempitsky V. 2018, Deep image prior: arXiv:1711.10925 [cs,stat].

[63] Richardson A. 2018, Seismic Full-Waveform Inversion Using Deep Learning Tools and Techniques, arXiv:1801.07232v2[physics.geo-ph]

[64] Zhu W Q, Xu K L, Darve E, Biondi B. and Beroza G C. 2021, Integrating Deep Neural Networks with Full-waveform Inversion: Reparametrization, Regularization, and Uncertainty Quantification, arXiv:2012.11149v3 [physics.geo-ph]

[65] Engquist B, Froese B D. 2014. Application of the wasserstein metric to seismic signals, Commun. Math. Sci., 12(5), 979–988.

[66] Pladys A, Brossier R, Li Y. On cycle-skipping and misfit functions modification for full-wave inversion: comparison of five recent approaches[J]. Geophysics, 2021: in press.

[67] Yang Y, Engquist B, Sun J Z. Application of optimal transport and the quadratic Wasserstein metric to full-waveform inversion[J]. Geophysics, 2018, 83(1): R43-R62.

Papers Published During Master's Studies

[1] **Zijian Wang**, Dan Li, Jianqiu Zhang, Dean Ta. A guided wave tomography method for Full Waveform Inversion based on recurrent neural network, *Chinese patent*, 202210622246.7.

Acknowledgement

I would like to express my gratitude to my supervisor, Associate Professor Dan Li, for his professional guidance. I'd want to thank him for providing me with a free and independent research environment and for inspiring my open scientific research ideas. The appreciation goes to my examiner MSc. Sahar Salimpour Kasebi at Turku as well.

Despite various difficulties in researching and improving the FWI technique, I eventually found a path for my efforts. I'd want to thank my supervisor once more, as well as Professor Jianqiu Zhang for his unflinching aid with my master's thesis. Their research attitudes are exemplary of what a true researcher should be.

My heartfelt gratitude goes to my coworkers and friends. I would like to thank Mr Xiaoxi Li and Mr Yuxuan Liu in particular for their assistance with my experimental efforts. I would also like to thank Dr. Alan Richardson at Trinity College Dublin for many critical discussions and for sharing the data in Chapter 4, Associate Professor Jing Rao at UNSW Sydney for helpful suggestions, Dr. Min Lin at University of Wyoming for offline training dataset, Dr. Yifang Li at Fudan University for supporting new computing methods, and Professor Gerard Gorman at Imperial College London for his generous help.

Finally, and most significantly, I want to thank my family for understanding my efforts, they never put any pressure on me and always encourage me. My love Miss Yaru Wang, this thesis is dedicated to you. Thank you, for your love and support.